



## HEK. VI. On the Dearth of Galilean Analogs in *Kepler*, and the Exomoon Candidate Kepler-1625b I

A. Teachey<sup>1</sup> , D. M. Kipping<sup>1</sup> , and A. R. Schmitt<sup>2</sup>

<sup>1</sup> Department of Astronomy, Columbia University, 550 W 120th St., New York, NY 10027, USA; [ateachey@astro.columbia.edu](mailto:ateachey@astro.columbia.edu)

<sup>2</sup> Citizen Science, private address

Received 2017 July 26; revised 2017 October 11; accepted 2017 October 14; published 2017 December 22

### Abstract

Exomoons represent an outstanding challenge in modern astronomy, with the potential to provide rich insights into planet formation theory and habitability. In this work, we stack the phase-folded transits of 284 viable moon hosting *Kepler* planetary candidates, in order to search for satellites. These planets range from Earth- to Jupiter-sized and from  $\sim 0.1$  to  $1.0$  au in separation—so-called “warm” planets. Our data processing includes two-pass harmonic detrending, transit timing variations, model selection, and careful data quality vetting to produce a grand light curve with an rms of 5.1 ppm. We find that the occurrence rate of Galilean analog moon systems for planets orbiting between  $\sim 0.1$  and  $1.0$  au can be constrained to be  $\eta < 0.38$  to 95% confidence for the 284 KOIs considered, with a 68.3% confidence interval of  $\eta = 0.16_{-0.10}^{+0.13}$ . A single-moon model of variable size and separation locates a slight preference for a population of short-period moons with radii  $\sim 0.5 R_\oplus$  orbiting at 5–10 planetary radii. However, we stress that the low Bayes factor of just 2 in this region means it should be treated as no more than a hint at this time. Splitting our data into various physically motivated subsets reveals no strong signal. The dearth of Galilean analogs around warm planets places the first strong constraint on exomoon formation models to date. Finally, we report evidence for an exomoon candidate Kepler-1625b I, which we briefly describe ahead of scheduled observations of the target with the *Hubble Space Telescope*.

**Key words:** planetary systems – techniques: photometric

### 1. Introduction

Moons present unique scientific opportunities. In our solar system, they offer clues to the mechanisms driving early and late planet formation, and several of them are thought to be promising targets in the search for life, as several are rich in volatiles (e.g., Squyres et al. 1983; Hansen et al. 2006) and possess internal heating mechanisms (e.g., Morabito et al. 1979; Hansen et al. 2005; Sparks et al. 2016). The moons of our solar system also demonstrate the great variety of geological features that may be found on other terrestrial worlds.

In this new era of exoplanetary science, it stands to reason that moons in extrasolar systems, so-called exomoons, should tell us a great deal about the commonality of the processes that shaped our solar system and may yield just as many surprises as their host planets before them. Just as the study of exoplanets has complicated our picture of planetary formation by revealing (for example) the existence of Hot Jupiters (Mayor & Queloz 1995)—worlds without solar system analogs—so too might moons show us what else is possible, and uproot conventional thinking about satellite formation mechanisms.

Galilean-sized moons ( $\sim 0.2$ – $0.4 R_\oplus$ ) are generally thought to be able to form in a variety of ways. For the regular satellites of Jupiter, the Galilean moons are thought to have condensed out of a circumplanetary disk, akin to planet formation within a protoplanetary disk (Canup & Ward 2002). This process is expected to limit regular satellites to a cumulative mass of  $\mathcal{O}[10^{-4}]$  that of the primary (Canup & Ward 2006). Higher mass-ratio moons, such as the Earth’s, evidently are also viable and may form from catastrophic collisions in the first few hundred million years of the solar system, coalescing from that collision’s debris (e.g., Ida et al. 1997). Finally, retrograde Triton is hypothesized to have originated from a capture event

via a binary exchange mechanism (Agnor & Hamilton 2006). Taken together, Galilean-sized satellites appear to have formed via at least three independent pathways within the solar system, and their existence around exoplanets can therefore be reasonably hypothesized.

Galilean-sized exomoons are challenging to detect using the transit method<sup>3</sup> for a number of reasons. First, the transit of a  $0.2$ – $0.4 R_\oplus$  moon across a Sun-like star results in a depth of 3–13 ppm, below the typical sensitivity achievable with *Kepler* (Christiansen et al. 2012). Second, the moon signal will almost certainly be found at each epoch in a different location with respect to the host planet, sometimes occurring before the transit, sometimes after, and at a different projected distance from the planet (Kipping 2011). Third, multiple moons around a single planet may wash out any transit timing (Sartoretti & Schneider 1999) or duration variations (Kipping 2009a, 2009b). The three-body motion, combined with the potential for overlapping disks (syzygies), makes accurate modeling of exomoon transits computationally demanding (Kipping 2011). Fourth, the long-period nature of plausible moon hosts means that relatively few transits are usually available. In this regime, a planet+moon light curve model has sufficient flexibility to almost always provide a superior fit to the limited data (Kipping 2013), thereby necessitating rigorous Bayesian approaches to model selection. Despite these challenges, the “Hunt for Exomoons with *Kepler*” (HEK) project has performed Bayesian photodynamical fits of  $\sim 60$  exoplanets to date (Kipping et al. 2012, 2013a, 2013b, 2014, 2015a), with no unambiguous detections and limits typically hovering around an Earth-mass.

<sup>3</sup> Note that the transit method is by no means the only method sensitive to exomoons; microlensing, for example, is another promising avenue (Bennett et al. 2014).

In this work, our project pursues a different approach to searching for evidence of moons, one that focuses on seeking a population of moons around a population of planets. Rather than pursuing individual limits that are then combined to constrain the population, we here approach the problem from a broad statistical perspective in order to directly measure the occurrence rate of moons,  $\eta_{\text{C}}$ . Resulting from this analysis, we identify a single exomoon candidate, Kepler-1625b I. We briefly describe its detection and vetting ahead of scheduled observations of the planet with the *Hubble Space Telescope* in 2017 October.

## 2. Stacking Exomoons

### 2.1. Phase-folding

The work presented here aims to exploit the power of stacking in order to search for exomoons. Stacking is a familiar technique to those studying exoplanet transits, who typically phase-fold a light curve upon the period. For a linear ephemeris, the transits align, leading to a coherent signal. It is important to stress that this act does not improve the signal-to-noise ratio (SNR). The amount of data before and after stacking is the same, with the only difference being that stacking assumes the ephemeris of the planet is known to infinite precision. Modeling the full unstacked light curve with a model conditioned upon the same ephemeris assumption would result in identical posteriors, and thus no improvement is achieved for the inference itself. Despite this, stacking is attractive because the signal's coherence means that full light curve modeling is unnecessary in the context of signal detection. Specifically, one may simply evaluate the weighted mean centered around the pivot point of the fold to achieve a detection, which is why the popular Box Least Squares (BLS) algorithm (Kovács et al. 2002) is a computationally efficient yet sensitive tool in conventional transit detection.

Stacking light curves in pursuit of exomoons is complicated by the fact that simply phase-folding light curves upon a linear ephemeris will lead to the moon appearing at different phases in each epoch. Despite the fact that the moon is not perfectly coherent, it is constrained to lie within a fraction of the Hill sphere radius (Barnes & O'Brien 2002) and this imparts some quasi-coherent properties into the phase-folded light curve. Simon et al. (2012) were the first to describe this possibility, where they argued that this quasi-coherence will lead to an increase in the photometric scatter in the temporal region surrounding the planetary event—an effect they dubbed “scatter peak.” A similar idea is discussed in Heller (2014), who instead considered looking for a slight photometric decrease in this temporal region. By considering the probability density of the moon’s sky-projected position, an effect dubbed the “orbital sampling effect” (OSE), Heller (2014) derives a simple formula for predicting phase-folded light curve shape in the presence of moons, enabling a simple approach to seeking exomoon shadows.

As with the case of a planetary transit, or indeed any kind of stacking, this approach does not boost SNR in any way. The data volume and quality are the same before and after the stacking. However, unlike the planet case, the shape of the phase-folded moon signal represents a washed-out depiction of the individual signals. Accordingly, the subtle individual variations in durations, positions, and shapes are lost, meaning

that stacking imposes a fundamental loss of information content, and therefore sensitivity.

A similar situation occurs when observing planetary transits with long exposures, such as the 30 minute cadence (LC) mode of *Kepler*, causing the shape of the transit to be slightly washed-out, thereby degrading the information content. It is for this reason that short-cadence (SC) *Kepler* data provides tighter constraints on transit times, despite the fact that both see the same SNR transit depth (e.g., see Kipping et al. 2013a and Kipping et al. 2014).

Accordingly, searching for exomoons in phase-folded light curves will always be less sensitive than full photodynamic fits—although precisely how much so has not been formally evaluated and would be sensitive to the specific planet/moon parameters. Despite this, phase-folding is attractive for its simplicity and as a pure detection tool—analogous to BLS for planet hunting.

One particularly attractive feature of phase-folding exomoons is that a sizable fraction of the quasi-coherent signal appears exterior to the planetary transit. Assuming the planetary transits are well-aligned and the duration is well-known, one may simply crop the planetary transit, leaving behind a pure exomoon signal. This greatly simplifies the analysis because the planet properties are not covariant with this signal.<sup>4</sup> For these reasons, we identify this out-of-transit phase-folded moon signal as the target signature in this work.

### 2.2. Planet-stacking

Unlike a simple planetary phase-fold, the quasi-coherent nature of the phase-folded moon light curve means that a large number of transits are needed to produce a predictable signal. At its core, the phase-folded moon signal depends upon the law of averages, and thus co-adding relatively few transits can lead to a phase-folded moon signal that is highly irregular and erratic. Without a characteristic and predictable shape, it is very difficult to convincingly argue that the signal is genuinely a moon, rather than some peculiarity of the data in those limited co-added events. Indeed, Heller (2014) argue that at least a dozen events are generally needed, such that  $N \gg 1$  and the averaging effect can become noticeable.

Unfortunately, *Kepler*’s primary mission lifetime of 4.35 years means that the long-period planets, where moons are most a priori expected to be viable, were only observed to transit a few times. Only in a small number of cases are there *Kepler* planets for which their period is long enough such that moons are dynamically stable for Gyr and we possess  $N \gg 1$  transit events within the 4.35 years of *Kepler* observations. This point seemingly excludes phase-folding as a viable exomoon approach, except for a few rare cases.

We devised an approach to solve this problem, inspired by the work of Sheets & Deming (2014). In that work, the authors not only phase-folded each planetary light curve, but also co-added different planets together. This allowed them to greatly increase the number of ensemble phase-folded signals, which in their case was used to boost the overall SNR. In many ways, this approach is reminiscent of a hierarchical Bayesian model (HBM; Hogg et al. 2010), but stacking the objects sacrifices the identities of each. While an HBM approach would be better

<sup>4</sup> Phase variations are not included in our model and thus cannot be covariant, nor should such phase variations persist given that our detrending algorithm will have largely removed them.

suit, in general, direct planet stacking is attractive for its simplicity, particularly if the objective is purely to test whether an ensemble signal even exists, rather than attempting to perform detailed characterization of said signal. Therefore, in the same vein, we decided to try stacking different phase-folded planet signals together, to solve the  $N \gg 1$  problem. We highlight that Hippke (2015) independently arrived at the same idea and published before our effort, although many differences exist in our actual implementations, as will become clear throughout this paper.

Co-adding different planets decreases the overall noise because we are extending the data volume upon which our inferences are conditioned. However, this approach is not guaranteed to increase the SNR because many of the objects co-added may not even possess moons, and thus their inclusion only dilutes the overall signal, rather than co-adding to it. Nevertheless, we can quantify the overall signal amplitude as being a combination of the occurrence rate and the moon radii. Even so, selecting a sample of planets that are expected, a priori, to be plausible hosts for large moons will be crucial for maximizing our chances of a successful detection and correspondingly deriving meaningful, physically constraining upper limits.

### 3. Target Selection

#### 3.1. Automated Target Selection

Not all exoplanets are equally likely, a priori, to yield an exomoon detection. At the most basic level, two questions guide our target selection process: (1) what is the largest stable moon plausible around a given planet (2) would this moon be detectable, given the current data in hand?

In this work, we estimate whether a detectable moon is plausible, following a similar approach to that adopted in previous HEK papers. Specifically, we employ the *Target Selection Automatic* (TSA) algorithm described in Kipping et al. (2013a).

To summarize, the algorithm first estimates a mass for each *Kepler* Object of Interest (KOI) using the maximum likelihood radius reported on the [NASA Exoplanet Archive](#) (Akeson et al. 2013) and the mass–radius relation defined in Kipping et al. (2013a). This is used to further estimate the extent of the planet’s Hill sphere. Moons are expected to have their lifetime limited by the time it takes to tidally spin out from the Roche limit to some critical fraction of the Hill sphere,  $fR_H$ . Using the expressions of Barnes & O’Brien (2002), this logic may be inverted to compute the maximum allowed moon mass,  $M_{S,\max}$ , which can survive for a fiducial age of  $t_\star = 5$  Gyr. For TSA, we set  $f = 0.9309$  for the optimistic case of a retrograde moon (Domingos et al. 2006). Note that we assume a single moon for stability estimates and tidal evolution timescales; the presence of multiple moons is expected to modify these values. However, because we do not know a priori how many moons may be present in a given system, it is impossible and impractical to apply more sophisticated stability estimates at this stage.

In order to compute  $M_{S,\max}$ , we must adopt a value for the ratio  $(k_2/Q)$ , which represents the efficiency of tidal dissipation. Whereas we simply adopted  $(k_2/Q) = 0.5/10^5$  in previous HEK papers, here we use an empirical relation based on the solar system. As shown in Figure 1, empirical estimates of  $(k_2/Q)$  for the Moon (Dickey et al. 1994), the Earth

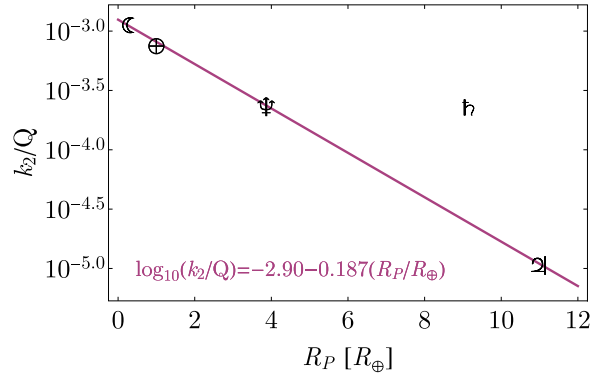


**Figure 1.** Relationship between the tidal property  $k_2/Q$  and planet size for the solar system bodies. When excluding Saturn, the remaining four points closely follow a power-law used in this work.

(Kozai 1968), Neptune (Trafton 1974), Jupiter (Lainey et al. 2009), and Saturn (Lainey et al. 2012) follow a power-law distribution versus planetary radii, except for Saturn. In this work, we invert this empirical relation (ignoring Saturn) to estimate  $(k_2/Q)$  for a given  $R_P$ . While we do not claim this to be a fundamentally general law, it at least provides a somewhat more reasonable estimate than the blanket fixed value assumed previously.

Once the maximum moon mass has been computed, it is then converted into a moon radius using the same mass–radius relation as before. Because target selection was conducted early on in the two-year duration of this research comprising this paper, it predated the more robust probabilistic mass–radius relation of Chen & Kipping (2017a), which is why that latter relation was not used for these calculations. We query the combined differential photometric precision (CDPP) of each host star (Christiansen et al. 2012), which, along with the maximum moon radius, allows us to estimate the signal-to-noise ratio (SNR) expected due to the moon.

For the SNR calculation, we estimate the phase-averaged signal amplitude using the so-called “orbital sampling effect” (OSE) described in Heller (2014). While these expressions formally assume a large number of transits, which is rarely true, they work well as an approximation for the signal strength marginalized over the moon’s phase, which is of course unknown to us a priori. The expected OSE flux decrease for the out-of-transit data is given in Heller (2014), from which we may integrate over the signal to compute the signal strength of the out-of-transit portion to be

$$S = \left( \frac{R_S}{R_\star} \right)^2 \frac{\sqrt{(a_{SP}/R_P)^2 - 4} - 2 \cos^{-1}(2R_P/a_{SP})}{\pi((a_{SP}/R_P) - 2)}. \quad (1)$$

The fraction on the right-hand side varies from about a quarter to a third for  $(a_{SP}/R_P)$  in the range of 5 to 100, i.e., it is a relatively gentle function. We therefore take the limit of large  $(a_{SP}/R_P)$ , giving

$$S = \frac{1}{\pi} \left( \frac{R_S}{R_\star} \right)^2. \quad (2)$$

The SNR may now be calculated by dividing this by the noise expected

$$\text{SNR} = \frac{1}{\pi} \left( \frac{R_S}{R_\star} \right)^2 \frac{\sqrt{T_{\text{Hill}}/0.25}}{\text{CDPP}_6} \sqrt{\frac{B}{P}}, \quad (3)$$

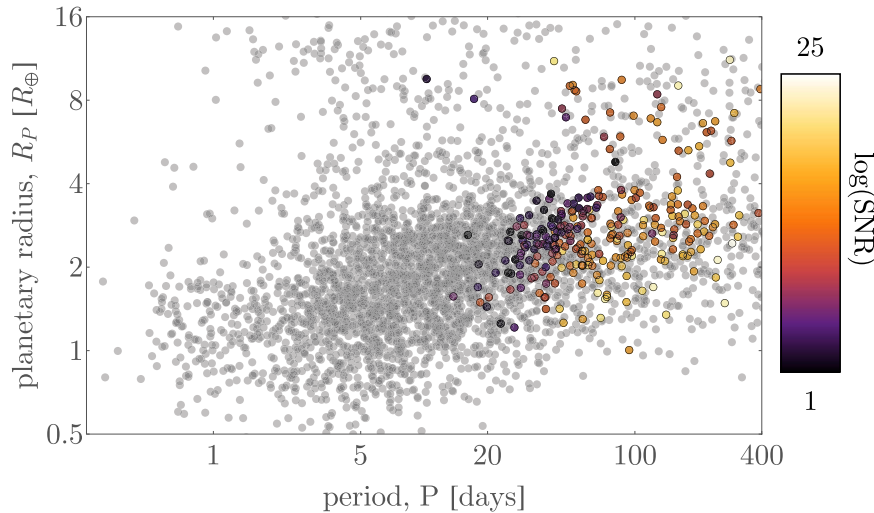


**Figure 2.** Location of the KOIs selected to search for nearby exomoons. The 966 colored points, color-coded by the SNR given in Equation (6), tend to be at relatively long orbital periods, where Hill spheres are larger. Points with a solid, black circle around them are the 347 KOIs found to pass our data quality vetting.

where  $B$  is the time baseline of observations, optimistically assumed to be the full Q1-17 baseline for these calculations and  $\text{CDPP}_6$  is the combined differential photometric precision on a 6 hr timescale. We may express the Hill time, assuming a simple circular orbit approximation, as

$$T_{\text{Hill}} = f \left( \frac{P}{2\pi} \right) \left( \frac{M_p}{3M_*} \right)^{1/3}, \quad (4)$$

which, when substituted in, leads to the  $P$  terms cancelling out, such that

$$\text{SNR} = \frac{(R_s/R_p)^2}{\pi} \left[ \frac{\sqrt{2Bf}}{3^{1/6} \sqrt{\pi} \text{CDPP}_6} \left( \frac{M_p}{3M_*} \right)^{1/6} \right]. \quad (5)$$

As discussed later in Section 6, we find that the OSE model overestimates the signal-to-noise for large  $a_{sp}$ , with numerical experiments showing that it is around a factor of three too high by the time we hit  $(a_{sp}/R_p) = 100$ . We therefore correct the SNR quoted above by dividing by a factor of  $\sim 3$ , which, along with by the  $\pi$  denominator, we simply approximate to a factor of  $\sim 10$  denominator, yielding

$$\text{SNR} \simeq \frac{(R_s/R_p)^2}{10} \left[ \frac{\sqrt{2Bf}}{3^{1/6} \sqrt{\pi} \text{CDPP}_6} \left( \frac{M_p}{3M_*} \right)^{1/6} \right]. \quad (6)$$

### 3.2. Applying to the Kepler Planetary Candidates

TSA was first run for this project in 2014 November, at which time 7305 KOIs were listed on the [NASA Exoplanet Archive](#). However, 27 were removed due to having some incomplete column entries. Of these, 4109 were not classified as a “false-positive” by the [NASA Exoplanet Archive](#), and thus were considered further. In order to calculate SNR, basic stellar properties are required, so we cross-referenced this list with the Huber et al. (2014) catalog, in which we were unable to find a match for 11 KOIs. Those were thus removed, giving us a total of 4098 KOIs that were then put through the TSA algorithm.

Due to the ensemble nature of our analysis, the total SNR is expected to be much greater than that of individual objects, and thus we can afford to use a relatively generous SNR cut. Accordingly, we elected to use  $\text{SNR} > 0.1$  and apply the

criteria that  $P < B/4 = 397.39$  days (to give three transits), leading to a sample of 966 KOIs outputted from the TSA procedure. These targets are visualized in Figure 2.

Because this work has taken several years to complete, some of the objects that were considered exoplanet candidates when we began are now considered false positives. In 2015 December, we elected to remove all KOIs that were either classified as “false-positives” at [NEA](#) or the probability of any false-positive scenario was in excess of 1%, as given by the values listed on [NEA](#). This filter removed 292 ( $\sim 30\%$ ) of the objects originally considered, reducing the number of usable KOIs from 966 to 674.

## 4. Data Processing Requirements

### 4.1. Overview

The objective of this work is to create a phase-folded planet-stacked out-of-transit light curve that may be used to search for evidence of exomoons. For the sake of brevity, we will refer to this light curve as the grand light curve, or simply GLC, in what follows.

We identify four unique and critical requirements for realizing this objective, specifically:

1. Removal of TTVs,
2. Very high-quality light curves,
3. Temporal rescaling,
4. Two-pass data processing.

We explain and discuss these requirements in what follows.

### 4.2. TTVs

In order to create an accurate phase-folded light curve of a sequence of planetary transits, it is necessary to ensure the transits accurately phase up. In the absence of transit timing variations (TTVs), this is a straightforward, simple linear ephemeris fold. However, the signal we seek, an exomoon, will always introduce a small TTV signal into the data (Sartoretti & Schneider 1999). Moreover, TTVs can be caused by other effects, notably perturbing planets (Agol et al. 2005; Holman & Murray 2005) and thus TTVs are observed to be fairly common ( $\gtrsim 10\%$ ) in *Kepler* planetary systems (Holczer et al. 2016).

Carefully removing these TTVs is crucial in creating an accurate phase-folded transit signal.

One approach might be to take the catalog of known TTVs from Holczer et al. (2016) and use these for corrections. However, there are several reasons why this is unsatisfactory for this work. First, in order to assess robust confidence limits, we require covariant, joint posterior distributions of the transit times and basic planet parameters, which were not derived in Holczer et al. (2016). Second, whenever possible, accurate phase stacking is aided by first conducting model selection between the TTV and linear ephemeris models, which itself formally requires computation of the Bayesian evidence—again, something not derived in Holczer et al. (2016). Third, the TTVs derived in Holczer et al. (2016) were conditioned on a different data set to that used in this work. More specifically, although both Holczer et al. (2016) and this work are based on *Kepler* photometry, our data-detrending methods are distinct, meaning that these differences should be expected to affect the TTV measurements to some degree. When one is ultimately seeking the discovery of a few parts-per-million signal, these conventionally minor issues cannot be ignored, and should be expected to influence the results.

For these reasons, we concluded that creating an accurate grand light curve was not possible without first deriving TTV posteriors ourselves for every system considered.

#### 4.3. Data Quality

There is a unique property of the phase-folded moon signal that has strong implications for the data-quality requirements, which is not conventionally an issue for planet analyses. The GLC signal is a phase-fold of the planetary transit, after removing TTVs, and thus at any given instant in phase, the moon actually only induces a transit-dip for some fraction,  $F$ , of the co-added light curves. Geometry demands that this fraction must always be less than one-half (i.e.,  $F < 0.5$ ) for all phase points occurring outside of the planetary transit signal. This is a key point that has a major implication: median binning kills the GLC signal.

This is extremely important, because median binning is a robust point estimate. The forgiving nature of median binning means that one can actually do a bad job of detrending some small fraction of the light curves (which represent outliers), yet still recover an accurate phase-folded signal. However, if one cannot use median binning, then one is forced to use mean-based estimates—which are sensitive to each and every transit co-added. In this case, even a single inaccurately detrended transit light curve will contribute to the phase-stacked signal. Once again, because we seek the detection of a signal with an amplitude of a few parts per million, this cannot be ignored and demands the highest levels of scrutiny and data quality.

We therefore establish that each and every transit used in our grand light curve must be verified to be of very high data quality, which, of course, greatly increases the time demands needed to complete such an analysis.

#### 4.4. Temporal Rescaling

When we finally arrive at an accurate phase-folded light curve for each planet, they must be combined into a single grand light curve. This is similar to the co-addition performed for occultations by Sheets & Deming (2014). In their case, each occultation has a distinct duration, and thus simply co-adding

the occultations would cause the signal to smear out and produce an averaged signal distorted from the true morphology. To overcome this, Sheets & Deming (2014) re-scaled each event by the known duration and then co-added, producing a more coherent signal. Just as with the occultations, each GLC signal will have a different velocity and impact parameter, and thus cause a different duration. However, the problem is actually worse because, unlike Sheets & Deming (2014), we do not know what the true duration of each event should be, due to the duration being highly sensitive to the semimajor axis of the moon(s), which are, of course, not yet discovered.

Ultimately, re-scaling will always be flawed because we can not know the semimajor axis of the moon prior to discovering it. A full hierarchical Bayesian model (HBM) would be an appealing way of approaching this problem, allowing each object to have a unique semimajor axis. However, because each planet would not satisfy  $N \gg 1$  transits, the OSE approximation would break down, and thus each system would require modeling with a full photodynamic simulation, such as that from LUNA (Kipping 2011). For five years, we in the HEK project have been conducting Bayesian regression of individual systems with LUNA, and the computational demands for even individual systems are formidable ( $\sim 30,000$  CPU hours per planet). Linking this into a full HBM would be extremely computationally challenging and was not a strategy we elected to pursue here.

Moreover, in this work, we ultimately hoped to find a signal that was visually evident in the final grand light curve, and thus not conditional upon the inferences of an HBM. While this does not maximize the information content of the final data product, we are motivated to follow this philosophy on the basis that the discovery of any novel phenomenon, which exomoons would represent, requires a much higher confidence than routine discoveries (Gould et al. 2004).

Accordingly, we seek a method of re-scaling that is “least-bad” and will maximize the expected signal coherence even when marginalizing our ignorance of the moon’s semimajor axis. One approach is that of Hippke (2015), who re-scaled by the duration of the planetary transit. The advantage of this is mostly simplicity; the duration is well-constrained and easy to understand. One downside of this is that, even if all the moons had the same semimajor axes, they would still lead to the grand light curve having a smeared out OSE signal because each system has different barycentric velocity and impact parameter across the star. Another approach, re-scaling by the Hill radii, is not possible because the exoplanet masses are unknown.

Instead, in this work, we argue that a better approach is to rescale the time axis into distance from the planet, in units of planetary radii. This can be accomplished by considering the original Seager and Mallén-Ornelas (2003) equation for the duration of a planet, under the assumption of circular orbits:

$$T_{23}^{14} = \frac{P}{\pi} \sin^{-1} \left( \sqrt{\frac{(1 \pm p)^2 - b^2}{a_R^2 - b^2}} \right). \quad (7)$$

If we let  $(1 \pm p) \rightarrow 1$  in the above, we recover the transit duration as defined when the center of the planet overlaps with the stellar limb,  $\tilde{T}$  (Kipping 2010a). Thus, at contact points 1 and 4, we can think of this instant in time as when a shell of radius  $p$  centered on the planet first starts to induce transit-dip features. By extension, we could adapt  $(1 \pm p) \rightarrow (1 + t'p)$  in the above, which would equal the duration of a shell of radius  $t'p$ , centered on the planet, to start/end creating transit-dip

features. In this way, we can think  $t'p$  as being the orbital distance of the moon at the instant in time when the transit begins/ends. Accordingly,  $t'$  represents the planet-moon distance in units of the planetary radius. This convenient form allows us to use the transit observables directly to convert from time into a physically motivated dependent variable via:

$$t' = \left[ \sqrt{b^2 + (a_R^2 - b^2) \sin^2 \left( \frac{2\pi}{P} (t - \tau) \right)} - 1 \right] / p. \quad (8)$$

If all of the moons shared the same  $(a_{SP}/R_P)$ , this would produce a coherent signal. In reality, we do not expect this statement to be true, but moons in the solar system do appear to be distributed log-uniformly with respect to this term (Kane et al. 2013). This approach means that we could model the resulting grand light curve, assuming exomoons followed a formulaic distribution for  $(a_{SP}/R_P)$ , such as a log-uniform.

In order to convert from  $t \rightarrow t'$ , we need estimates for the impact parameter and scaled semimajor axis. Because our data are not strictly the same as those used for the inferences quoted elsewhere, a self-consistent analysis demands we derive these estimates ourselves, which forms another requirement for our work.

While our conversion equation assumes a circular orbit, if we fit the data under the same assumption, the relative estimate is at least self-consistent. Further, eccentric planets have smaller regions of stability for exomoons (Domingos et al. 2006) and have likely experienced scattering, which decreases the chances for moons further (Gong et al. 2013). Thus, if the planet is eccentric, the incorrect conversion is likely irrelevant because such planets likely do not contribute OSE-signals into the grand light curve anyway.

#### 4.5. Two-pass Detrending

In this work, we use the CoFiAM algorithm to detrend the *Kepler* light curves. We direct the reader to Kipping et al. (2013a) for details on the algorithm, but essentially its goal is to remove long-term trends without introducing any power, in a Fourier sense, at periodicities less than the transit duration. This requirement ensures that any signals with a timescale approximately equal to or less than this duration will not be distorted by the detrending process itself, because a transit can be thought of as a Fourier series with the lowest frequency being that of the duration (Waldmann et al. 2012). Accordingly, both the planet and moon transits are preserved, in contrast to polynomial-based methods that introduce power at all frequencies.

We do not even attempt to remove high-frequency noise, but it is monitored by measuring the autocorrelation at the cadence-lag and used to optimize both the harmonic filtering and subsequent identification of “bad transits,” which are typically rejected.

A disadvantage of CoFiAM is the requirement for a precise estimate of the time and duration of all transits in the time series. For this reason, it generally is not useful for blind searches for exoplanet transits. However, when seeking exomoons, this requirement is generally true; indeed, CoFiAM should really be thought of as an exomoon-optimized detrending method more than anything else.

As before, transit times and durations are often available for the planets under consideration, but those times and durations were conditioned on a different data detrending. In order to

make our analysis self-consistent, we must derive these times and durations ourselves. However, herein lies a Catch-22: to derive these times, we first need detrended data, which itself first requires the times. To tackle this, we use two passes to iterate onto the best solution. The first pass uses the literature values for the times and duration of the transits and then performs CoFiAM. The second pass takes the times and durations inferred using the first-pass data product, then performs a new round of detrending with CoFiAM. This approach ensures both self-consistency and reliability in our estimates, and also provides several opportunities to vet the data quality, ensuring only the highest-quality light curves are used in the final analysis.

## 5. Data Processing Pipeline

### 5.1. Overview

As motivated in Section 4, we require a joint posterior distribution for the times and basic transit parameters of all planets used for the final analysis. Using a two-pass approach to detrending-fitting ensures that our inferences are self-consistent and conditioned upon the actual data product used in this work. In this section, we provide a detailed explanation of the data-processing steps comprising each pass, which are tailored to the specific and unique goals of the two. An illustrative overview is provided in Figure 3 for reference.

### 5.2. Pass A

#### 5.2.1. Goals of Pass A

We first re-assert that the primary goals of Pass A are to: (1) derive transit times for each transit and (2) derive the transit duration for each planetary candidate. These products may then be used to conduct a second detrending later in Pass B, because our detrending procedure (CoFiAM) requires the times and durations for execution.

These two objectives necessitate detrending of the data first, because we do a covariant detrending plus inference model that requires an HBM, which is beyond the scope of this work for reasons described earlier.

For Pass A, we make all decisions regarding data quality based upon whether we conclude that these two goals can be achieved. For example, in cases where there is plenty of out-of-transit data, but no in-transit, these would be rejected in Pass A (but can be picked up later in Pass B because such signals may still contain exomoon transits). Ultimately, defining a clear and independent objective for each pass allows us to optimize required steps.

In what follows, we describe the different stages of data analysis that are performed in Pass A.

#### 5.2.2. Stage A1

The first step is simply to download the *Kepler* Simple Aperture Photometry (SAP) for each target. We wrote a shell script to step through the target list (see Section 3), creating a local directory for each KOI. Using a WGET script, any and all of the target’s LC data is then downloaded from MAST (from <http://archive.stsci.edu/pub/kepler/lightcurves/>) and saved in the appropriate directory. As the data were downloaded in batches, the *Kepler* Science Operations Center data processing pipeline used for these files varied from 9.0.3 (2013

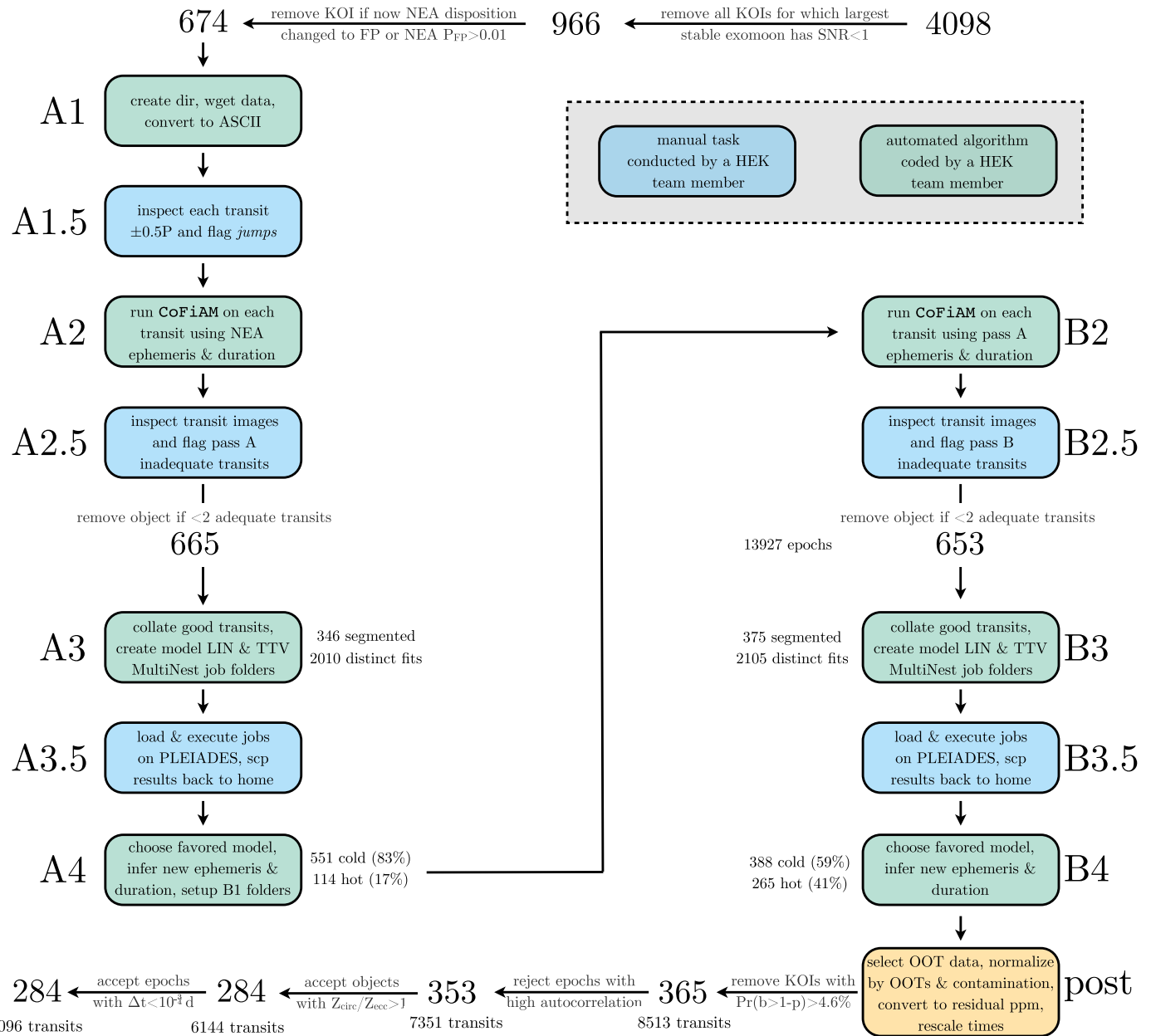


**Figure 3.** Schematic diagram of the pipeline used to process the *Kepler* SAP photometry, and ultimately to construct the grand light curve. We color code the manual steps in blue and the automated steps in green. The left column broadly describes Pass A, and the right column Pass B. For details on each step, we direct the reader to the relevant subsection in Section 5.

April 18 creation date) to 9.2.23 (2014 November 18 creation date).

Pre-prepared template detrending scripts are copied into each target directory. As with previous HEK papers, we use CoFiAM to perform our detrending. We direct the reader to Kipping et al. (2013a) and Kipping et al. (2013b) for details on the algorithm. We stress here that the algorithm is designed specifically for the exomoon problem and requires detailed initial information—such as planetary periods, transit times, and durations—in order to work, which ultimately again explains why the two-pass data-processing strategy is used.

We use the *Kepler* SAP time series throughout because this time series has less chance of having unintended artificial signals present than the Pre-search Data Condition (PDC) time series (Smith et al. 2012; Stumpe et al. 2012), which has been subject to data-massaging techniques already.

### 5.2.3. Stage A1.5

We manually inspect an image of each and every transit light curve epoch, centered upon the time of transit minimum expected from a linear ephemeris and including  $\pm 0.5$  orbital periods of data either side. We never attempt to stitch different quarters together, and instead simply reject any datum that occurs in a different quarter than that of the transit epoch under consideration. As before, ephemeris parameters are taken from the NASA Exoplanet Archive for this task.

At each epoch, we identify if any sharp jumps, exponential flux variations, or other anomalous light curve features exist in the data. This process is performed using the criterion of whether or not CoFiAM would be able to fit the light curve variations. The aim is to keep a sufficiently long series of data to perform a robust detrending, but clip out patterns that may

degrade the performance of CoFiAM, with an appreciation for the basis set that CoFiAM employs.

We initially pursued a variety of automated metrics for this purpose, such as standard deviation, autocorrelation, and linear trends. However, we found that a wide variety of anomalous features survived and thus deceived these simple metrics. Rather than creating an ever-larger battery of metrics, for which there would still be no guarantee of completeness, we instead acknowledged that the human eye remains an unparalleled tool in quickly identifying anomalies in time series data.

Anomalous features are flagged by saving the instant in time just before/after the feature, depending on whether the feature occurs after/before the time of transit minimum. This process required approximately 60 hr of human labor in total.

We note that the provided cotrending basis vectors are derived from the study of common trends between stars; in an ideal world, they would provide a perfect removal of instrumental effects. However, they do not remove stellar variations, which must also be removed to apply our method. We therefore opt to use CoFiAM, not only because it is optimized for the moon problem, but also because it accounts for both instrumental and astrophysical trends in a single step, which reduces the chances of artificially injecting or removing a moon signal. It is preferable to have fewer manipulations of the data, and by setting a strict frequency limit to protect the transit Fourier decomposition signal, we ensure that our method does not overfit out small signals of potential interest.

#### 5.2.4. Stage A2

Stage A2 involves the first detrending of the light curves. As mentioned earlier, this is performed automatically using CoFiAM and the list of anomalous features to ignore (found manually in stage A1.5). While details of CoFiAM can be found in Kipping et al. (2013a, 2013b), we point out some general options selected for the execution in this paper.

The outlier threshold is set to  $3\sigma$  from a 20 point moving median. Before detrending, all planetary transits are removed with an exclusion window of  $\pm 0.6T_{14}$  for all events (half a duration either side plus 20% buffer), including the object of interest.

Each transit is detrended separately, using  $\pm 0.5P$  of the data surrounding each event. If the transit epoch has any associated anomalous flux changes, as discussed in stage A1.5, then points beyond these times are also cropped.

Periodic functions described by a sum of harmonic cosines are explored from twice the data baseline down to twice the transit duration, with a cap of 30 harmonics (beyond which we tend to encounter numerical instabilities). This choice ensures that CoFiAM does not disturb the shape of the planetary transit in a Fourier sense (Waldmann et al. 2012).

Each model is regressed to the data, then ranked by the local autocorrelation, as computed using the Durbin & Watson (1950) statistic (DW) on the timescale of the LC cadence, with the lowest autocorrelation being favored. The favored model is then applied to original time series, re-including the planetary transit of interest. The final light curve is saved with a  $\pm 6.66T_{14}$  gap either side (which is the local timescale used for the DW calculation).

Finally, an image of every detrended transit is stored along with the best DW statistic.

#### 5.2.5. Stage A2.5

This is the second manual stage in pass A, where we manually identify “bad” transits. In some rare cases, CoFiAM fails and produces a light curve that cannot be used for fitting, due to visually evident trends remaining in the data. For example, if we missed a location of an anomalous flux variation in stage A1.5, CoFiAM may be trying to detrend sharp features with a smooth cosine function, producing a poorly detrended light curve. Manually going through the light curves in this way is essentially a second check of the data quality, catching any missed anomalies from earlier.

In general, these assessments are made by one of us searching for any visually evident trends that would significantly impede our ability to fit the light curves to determine  $T_{14}$ . A bad transit does not necessarily have a poor DW statistic, although that tends to be a common scenario. Because we anticipate a second pass, we can be generous in considering acceptable data qualities at this stage. This acceptance level is non-constant because we try to allow KOIs displaying very frequent bad transits to have at least a few transits that can be used for fitting in stage A3. On the other hand, if a KOI has many clean transits, we apply more stringent conditions in assessing data quality. Finally, we note that assessments are generally based on SNR of the transit, not the raw wiggles in the data, but the relative size of those wiggles compared to the transit. In cases of very low SNR, where the transit is not visible in a single epoch, we work under the assumption that sometimes data will wiggle up and sometimes down, but we must trust that, on the average, there is power (thus we try to allow for almost anti-transit-like features in the interests of being unbiased and balanced). In such cases, our criterion switches from trying to make a good measure of the transit duration to simply avoiding “catastrophic” detrendings.

In addition to a “bad-transit flag,” we also use a “sparse flag” for transits where there is insufficient in-transit data (or none at all). In some rare cases, a third type of flag was used, the “missing flag,” where the data are well-detrended and we have good temporal coverage, but a transit that should be visually obvious (given the transit depth) is missing in the data. We consider these cases to be most likely due to an erroneous transit ephemeris on the [the NASA Exoplanet Archive](#).

If fewer than two good transits remain for a KOI, the object is removed from our sample as being a useful object. In total, this removes nine KOIs, dropping our sample from 674 to 665 KOIs. It should be noted that any rejection of bad data, manual or automated, injects additional uncertainty into the occurrence rate of exomoons calculated in this work, which is, strictly speaking, of unquantifiable magnitude. If there is any correlation between unusable transits and the presence of moons, the calculation could be particularly affected, but this is impossible to measure because the bad transits are, by definition, unusable for exomoon characterization. We proceed under the assumption that bad data result from instrumental effects that are distributed randomly across the data set.

#### 5.2.6. Stage A3

The third stage is an automated shell script that begins by stitching the good transits together for each KOI into a single file. Our script then creates two directories for a linear ephemeris model fit,  $\mathcal{H}_{\text{LIN}}$ , and a transit timing variation model fit,  $\mathcal{H}_{\text{TTV}}$ , to be fed into MULTINEST (Feroz & Hobson 2008;

Feroz et al. 2009). The script then queries the orbital period,  $P$ , and time of transit minimum,  $\tau$ , from the [NASA Exoplanet Archive](#) database to construct priors for these terms. In the case of model  $\mathcal{H}_{\text{LIN}}$ , the prior on both terms is uniformly centered on the [NASA Exoplanet Archive](#) reported value with a  $\pm 1.0$  day window. For model  $\mathcal{H}_{\text{TTV}}$ , the period is treated as a fixed parameter, with the individual transit times following a uniform prior centered on the expected time of transit for a linear ephemeris, again with a  $\pm 1.0$  day window. The choice of the  $\pm 1.0$  day window is essentially arbitrary, but assumes that transit timing variations larger than one day are highly unlikely in the region between 0.1 and 1.0 au (cf. Holczer et al. 2016), who find  $<0.3\%$  of their sample have TTV amplitudes larger than one day). A larger window will unnecessarily increase the time it takes to explore the parameter space, while a smaller window tailored to the linear ephemerides of each planet could result in a bias against finding large TTVs.

For model  $\mathcal{H}_{\text{LIN}}$ , the basic free parameters are  $P$  and  $\tau$ , two quadratic limb darkening terms (we use the  $q_1$  and  $q_2$  prescription from Kipping 2013), the ratio-of-radii,  $p$ , the impact parameter,  $b$ , and the stellar density,  $\rho_\star$ . Uniform priors are adopted for all except  $\rho_\star$ , which follows a log-uniform prior. This gives a total of  $d = 7$  free parameters, which is easily handled by MULTINEST. For model  $\mathcal{H}_{\text{TTV}}$ , the period is treated as fixed, removing one degree of freedom, but then each transit epoch has a unique  $\tau$  parameter (same prior as  $\mathcal{H}_{\text{LIN}}$ ), giving us  $d = 6 + N$  free parameters. For  $d \gtrsim 20$ , the performance of MULTINEST is severely impeded and global fits are not possible.

A common approach is “templating,” where one folds the transits, creating a template that is then regressed to the individual epochs (e.g., Holczer et al. 2016). This approach underestimates measurement uncertainties because it ignores the covariance between the transit shape parameters and the individual transit times. Rather than underestimating errors, we prefer to overestimate them and so adopt a different strategy. Instead, we split up our light curves in segments of  $\sim 10$  epochs each, providing a manageable number of free parameters for each. The downside is that each segment is not able to utilize information about the global transit shape learnt from other segments, and so the uncertainties will be larger (but more robust) than templating. Accordingly, in stage A3, our script automatically segments the data where necessary.

We find that a total of 346 out of our sample of 665 KOIs require segmenting, whereas the rest are treated in a single fit due to the tractable number of epochs available.

#### 5.2.7. Stage A3.5

Stage A3.5 was primarily performed using NASA’s Pleiades cluster, and essentially involved loading, compiling, executing, and then retrieving the over 2000 light curve regression jobs required. In total, we estimate that approximately  $\sim 100,000$  CPU hours were used during this phase of the analysis and spanned several months of wall time.

#### 5.2.8. Stage A4

In the fourth stage, we segue into pass B by laying the ground-work needed using the results from our light curve fits. The first task is to decide for each KOI whether it is dynamically “hot” or “cold,” by which we mean whether  $\mathcal{H}_{\text{LIN}}$  model (cold) or  $\mathcal{H}_{\text{TTV}}$  model (hot) is preferred. In cases

where the fits were completed using a single segment, the evidences from MULTINEST can be directly used to compute the Bayes factor and rigorously assign the preferred model. For segmented models, direct evidence calculation is not possible because the TTV model has multiple copies of the same parameters for the transit shape. Instead, we use weighted linear regression to find the maximum likelihood linear ephemeris through the posterior transit times, and then inspect the residuals for evidence of TTVs. This is simply done using a  $p$ -value test searching for an excessive  $\chi^2$  (cut off used was  $3\sigma$ ).

Formally, model assessments using a  $p$ -value are incorrect because they are never actually compared to another model. More precisely, the  $p$ -value test is prone to inferring significant evidence for the alternative hypothesis even in cases where it should not. For example, excess noise from other sources or a single poor measurement could lead to the  $p$ -value test favoring the TTV model erroneously. Let us consider the effect of this by imagining a linear ephemeris fit to a set of transits with the TTV model. The times of transit and basic transit parameters will all still come out formally correct, just with inflated uncertainties. Giving each epoch a free transit time still allows us to recover the original linear ephemeris solution. Therefore, despite the  $p$ -value’s tendency to overestimate significance, this merely acts to conservatively inflate our uncertainties and does not formally invalidate our inferences.

In total, we find 551 of the 665 KOIs are cold, with the remaining 114 being dubbed hot. For later comparison, we point out that one might expect pass B to increase the hot fraction due to the improved detrending and thus greater sensitivity to even small TTVs.

Stage 4 ends by duplicating all of the KOI folders into a new directory with a small text file recording the favored model and ephemeris parameters. The transit duration is also recorded in this file, where  $\mathcal{H}_{\text{LIN}}$ -favored KOIs are computed directly from the joint posteriors, and  $\mathcal{H}_{\text{TTV}}$ -favored KOIs from a weighted sum of each segment’s marginalized credible interval for the duration.

### 5.3. Pass B

#### 5.3.1. Pass B Goals

Before describing each data-processing step for pass B, we first re-assert the objectives, which represent the backdrop against which all decisions in pass B are framed.

Ultimately, the data product from pass B should be high-quality, cleaned light curves with accurate estimates of the transit times and basic parameters needed for stacking and rescaling. Our tolerance for poor-quality light curve is necessarily more stringent here because, unlike pass A, there is a second chance for these light curves and they have to be of sufficient quality for stacking by the time pass B is complete.

#### 5.3.2. Stage B2 and 2.5

Downloading the data (stage 1A) and removing jumps (stage A1.5) need not be repeated because the raw data product is unchanged. Accordingly, we skip straight to stage B2. Mirroring stage A2, we detrend the SAP light curves using CoFiAM, but now using the duration and transit times determined earlier in stage A4 (specifically, we use the maximum a posteriori values).

In stage 2.5, we again inspect these light curves visually for poorly detrended examples and find that 12 KOIs end up with fewer than two usable transits after this process. Removing these objects reduces our sample from 665 to 653 KOIs.

### 5.3.3. Stage B3 and 3.5

As with stage A3, stage B3 collates the good transits and sets up folders for models  $\mathcal{H}_{\text{LIN}}$  and  $\mathcal{H}_{\text{TTV}}$ , ready for fitting with MULTINEST. Once again, this results in just over 2000 distinct jobs to run, with 375 of the KOIs being segmented.

Unlike stage A, we here allow the light curve model to account for any known blending from nearby sources. These are collated from Everett et al. (2015), Kolbl et al. (2015), Adams et al. (2012), Adams et al. (2013), Dressing et al. (2014), Law et al. (2014), and we use *Kepler*-converted magnitudes to estimate the appropriate contamination factor for each band. These blending factors are treated as Gaussian priors, with a standard deviation set by the uncertainty on the converted magnitude. In total, 39 of the targets required a blending term to be included.

In stage 3.5, we again load, compile, execute, and retrieve these runs on the NASA Pleiades cluster, requiring another round of 100,000 CPU hours and several months of wall time.

### 5.3.4. Stage B4

Finally, stage B4 repeats stage A4 with the new light curve fits, performing model selection using the same framework described earlier. After completion, we found that the fraction of cold KOIs decreased, as expected, from 83% to 59%, giving 265 hot KOIs in our sample. In this work, these TTVs purely represent a nuisance, but we acknowledge that this data set represents a rich and interesting catalog for others in the community. We therefore make all of the transit times, for both the hot and cold samples, publicly available at [github.com/alexteachey/TTV\\_posteriors](https://github.com/alexteachey/TTV_posteriors).

For each KOI, we export the maximum a posteriori transit fit and corresponding vector of out-of-transit baseline fluxes (OOTs), which are found by linear minimization of the maximum a posteriori model and the data (this is actually done on the fly during every regression step, following the approach using by Kundurthy et al. 2011). These OOTs will be useful later for stacking the final light curves.

## 5.4. Post-processing

In post-processing, for each KOI, we aim to export a single file containing a phase-folded light curve suitable for planet-stacking. First, the transit times are removed using the favored model and the maximum a posteriori parameter vector. Next, the planetary transit is removed by excluding all data that fall within the  $2\sigma$  upper limit of the derived full duration,  $T_{14}$ . Each epoch is then corrected for any residual DC power detected by the OOT vector regressed during Stage B4. Global blending factors, as well as quarter-to-quarter aperture flux contamination factors are corrected for, following the approach described in Kipping & Tinetti (2010).

Next, we subtract unity from the normalized fluxes and multiply by 1,000,000 to create a ppm residual light curve for each object. Finally, the time column is converted to  $t'$  using Equation (8) and the maximum a posteriori transit parameters derived from the preferred model regressed in Stage B4.

## 5.5. Filtering

Before stacking these planets together, we first remove KOIs and individual transits that fail to satisfy several criteria. First, we require a  $2\sigma$  confidence that the planet is not a grazing event, which would mean that  $b > (1 - p)$ . Grazing events have degenerate planetary radii and could be far larger in size, potentially even a false positive. Erring on the side of caution, we remove any such KOI that filters out 288 KOIs, leaving us with 365 targets.

We next test for excessive autocorrelation using the DW metric. For each transit, we generate 10,000 mock realizations where the data are drawn from perfect normal distributions at the exact same sampling observed in the data and the reported uncertainties. We use these synthetic transits to generate an expected distribution for the DW metric and flag any transits for which the real DW metric is more than two standard deviations away from our synthetic population. If a KOI has 50% or more of its transits flagged in this way, the entire KOI is dropped from the sample. This filtering removes a further 12 KOIs.

Next, we compare the transit-derived stellar density (which assumes a circular orbit) to an independent estimate, in order to exploit the photoeccentric effect (Dawson & Johnson 2012; Kipping et al. 2012) to infer a minimum eccentricity,  $e_{\min}$ , of each KOI (Kipping 2014). We draw a random sample from the transit derived posterior found in stage B4 and divide it by a random sample drawn from the KOI's corresponding stellar density posterior derived in Mathur et al. (2017). This ratio is then converted into a minimum eccentricity using Equation (39) of Kipping (2014), and the process is repeated until we have derived 40,000 posterior samples for  $e_{\min}$  for each KOI. For each KOI, we also construct a prior for  $e_{\min}$  based off the prior used in the transit fits and Mathur et al. (2017) distribution.

We next evaluate the Savage-Dickey ratio between the posterior and the prior to estimate the Bayes factor,  $Z_{\text{circ}}/Z_{\text{ecc}}$ . We find that 284 KOIs have  $Z_{\text{circ}}/Z_{\text{ecc}} > 1$ , implying a near-circular orbit, whereas the other 69 KOIs are rejected for further analysis on the basis that eccentric planets likely result from scattering that would disrupt moon systems (Gong et al. 2013). We plot  $e_{\min}$  as a function of the Bayes factor in Figure 4.

Finally, we elected to remove transits for which we are unable to measure the transit time to within a precision of  $10^{-0.75}$  days, chosen to remove unconverged posteriors given the prior width, which is necessary to ensure we are able to reasonably phase-fold transits together. This did not change the number of KOIs from 284, but did reduce the number of transits in our sample from 6144 to 6096.

## 5.6. Constructing a Grand Light Curve

With each target now having a fully processed phase-folded light curve, we are finally ready to stack different targets together to create a grand light curve. This stacking can be across all 284 surviving targets, or a subset of them, as explored later. Although we describe here the case for the complete ensemble, the planet-stacking methodology is the same when dealing with subsets.

Across the 284 KOIs, we have 6096 unique transits comprising of 364059 photometric measurements. The rescaled times are well-described by a half-normal distribution

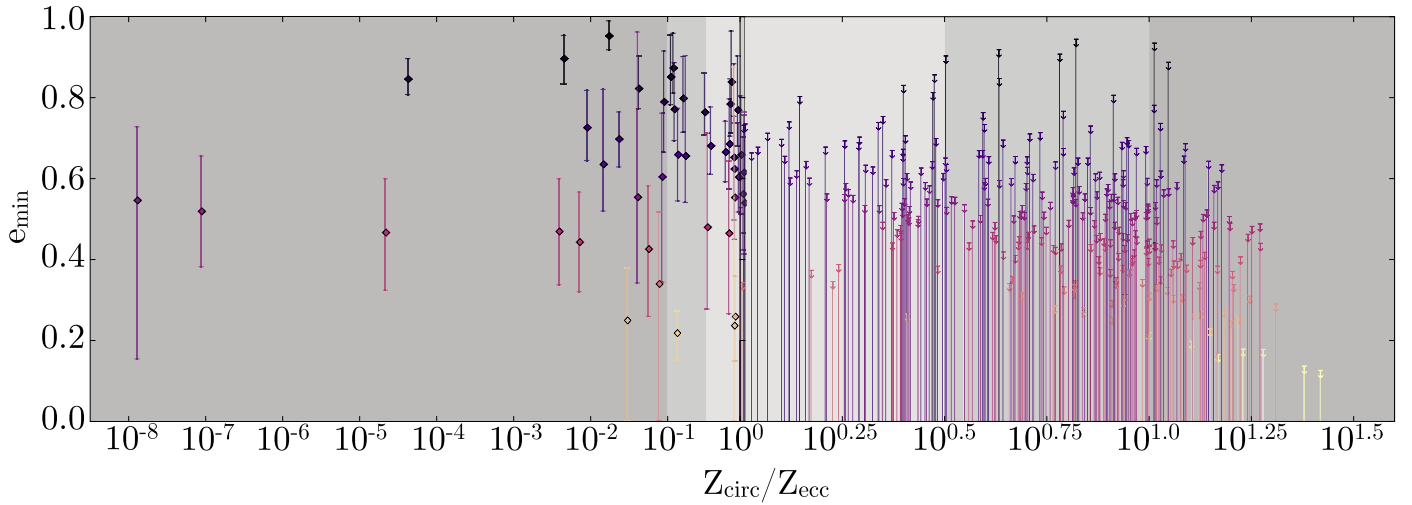


**Figure 4.** Minimum eccentricity of 353 KOIs derived using the photoeccentric effect as a function of the Bayes factor for a circular vs. eccentric orbit. KOIs to the right of unity are depicted as upper limits on eccentricity, whereas we plot  $1\sigma$  credible intervals for the others. The 284 KOIs favoring a circular orbit are considered further as viable exomoon candidates in this work.

with a standard deviation of 113. We elect to remove any points that fall outside of the range  $t' > 150$ , leaving us with 309,750 points.

The grand light curve photometry shows no evidence for correlated noise structure, as expected from averaging so many independent data sets together. This is verified in Figure 5, where we plot the root mean square (rms) of the time series as a function of bin size, which displays excellent agreement with the expected  $N^{-1/2}$  scaling.

Dividing the fluxes by their formal reported uncertainties, we find that the robust rms (given by 1.4286 multiplied by the median absolute deviation) equals 1.09, indicating only a small amount of extra noise above the reported uncertainties. We re-scaled the errors by this factor and then performed  $3\sigma$  clipping, removing just under one percent of the points. The final time series is found to have a standard deviation of 5.1 ppm when binned to a scale of  $\Delta t' = 0.5$ .

## 6. Modeling

### 6.1. Choosing a Modeling Formalism

In addition to manipulating the *Kepler* data to construct the grand light curve, we also require the ability to model its shape, as a function of various exomoon parameters of interest.

There are two possible avenues to modeling the grand light curve. The first is to model the individual systems, then combine them to create an ensemble model, and the second is to use a model describing the ensemble from the outset. The latter approach describes the model proposed in Heller (2014) and later modified in Heller et al. (2016), who refer to this model as the “orbital sampling effect” (OSE). The great advantage of this approach is that one can employ analytic expressions described the ensemble signal without having to laboriously simulate each of the individual systems and then combine them later. Thus, in principle, the OSE approach has the advantage of speed and being more straightforward in application. Indeed, this was the model used in Hippke (2015).

The alternative approach would be to use a detailed “photodynamical” light curve simulator, such as LUNA (Kipping 2011), to predict the light curve of each system with some trial set of moon parameters and later combine them to

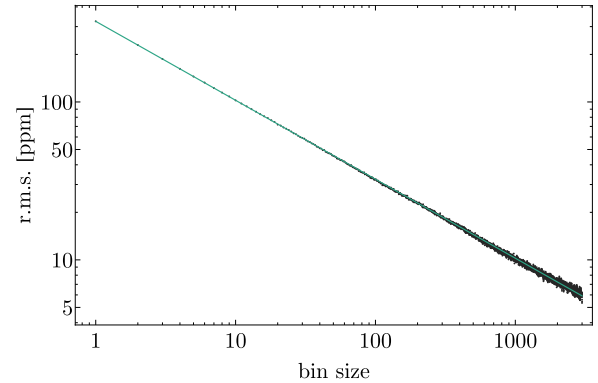


**Figure 5.** The rms of the grand light curve as a function of bin size, demonstrating the expected  $N^{-1/2}$  scaling of white noise.

produce a grand model. Photodynamics, a test first coined in Carter et al. (2011), refers to a light curve simulator that evolves a planetary system at each time step and computes the corresponding shadows cast onto the sky-projected stellar disk. Unlike the OSE model of Heller (2014), this model is not specific to phase-folded events, but can, of course, be easily used to simulate such a case by simply folding the final predicted light curve.

In general, LUNA provides a physically detailed light curve simulation, but that comes at the expense of greater computational cost than the simple closed-form expressions of OSE. For these reasons, if the accuracy of OSE is validated, it would be far simpler (and thus preferable) to employ the OSE formalism for our model fits of the grand light curve. However, after photodynamical testing of the OSE predictions and consideration of the specifics of our problem hand, we came to the conclusion that OSE would not be an accurate modeling tool for our data product. In particular, we argue that three key barriers prevent us from directly using the OSE models to describe our grand light curve:

1. Inter-population variation,
2. Heteroscedastic weighting,
3. Laplace resonances.

We briefly describe these three reasons in what follows.

### 6.1.1. Inter-population Variation

The OSE model is derived assuming that one co-adds many transits of the same planet-moon system i.e., that the basic parameters of the system are not changing. However, in our case, we co-add different systems together that have distinct planet and moon parameters. For example, in our Galilean moon fits, we assume that the moons have inclinations representative of Io, Europa, Ganymede, and Callisto, but each planet’s moon system will have unique moon inclinations, despite being drawn from a common underlying distribution. While we could co-add many OSE signals modeled individually with the corresponding parameters, each OSE curve would be modeling only a small number of transits and thus would be formally invalid—because it is, by definition, an ensemble model. Without detailed investigation, it was unclear that one could simply co-add across a population in this way and recover the correct phase stacked signal and thus we preferred to use LUNA which provided an accurate model of the individual events.

### 6.1.2. Laplace Resonances

A subtle and minor point of concern was dealing with the Laplace resonance in the OSE framework when modeling Galilean analogs. In LUNA each individual moon transit is generated and thus we are able to assign relative phases between the satellites such that they reside in not only the correct mean motion resonance but also share the Laplace resonance in terms of their mutual phases:  $\pi = \lambda_{\text{Io}} + 3\lambda_{\text{Europa}} + 2\lambda_{\text{Ganymede}}$ . In contrast, the OSE framework never models the individual events, only the ensemble, and we were unable to demonstrate that OSE was correctly accounting for such a phase lock.

### 6.1.3. Heteroscedastic Weighting

Finally, OSE is an average of light curves; by definition, this means each light curve is given precisely the same weight. Second, each light curve contribution is assumed to be uniformly and densely sampled. Our real data products do not satisfy such constraints, because we first co-add the different planets, using weights based off the root mean square of the photometric residuals. Second, light curves are not uniformly sampled—they feature data gaps and removed outliers, as well as being non-uniformly transformed in time via our temporal re-scaling. Data gaps, integration time effects (Kipping 2010b), and re-scaling are easily accounted for before applying any co-addition, because LUNA models individual events, enabling us to ensure our model is representative of the data.

## 6.2. Photodynamic Look-up Tables (LUTs)

As a result of the myriad of complicated effects influencing the final model, yet the relative low-dimensionality of the model itself, we elected to build a grid of pre-computed models that accounted for all of the effects described above. For each KOI, we took the maximum a posteriori transit parameters from the planet-only fits (using the favored model) and generated a planet+moon light curve using LUNA with the same planet parameters but adding in one or more moons. The model curve

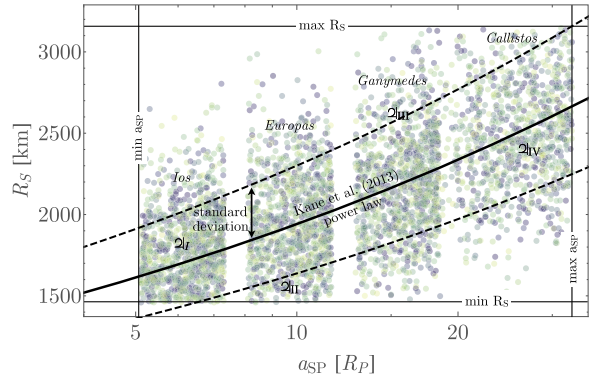


**Figure 6.** One thousand randomly generated Galilean moon system analogs, using the method described in the main text. Each color represents a unique system comprised of four moons.

is generated at precisely the same cadence as the data used for the planet-stack and accounts for the long-cadence integration time using one-minute numerical re-sampling (Kipping 2010b). After all of the KOI model light curves have been computed for a specific choice of underlying moon population, they are co-added with the same weighting used for the real data. In other words, we inflict precisely the same transformations upon the model as we do the data, to ensure a like-for-like comparison at the end.

### 6.2.1. Galilean Analogs

The moons are generated in two ways. The first case was for a Galilean analog. Here, we assume that four moons orbit each KOI with properties resembling those of Io, Europa, Ganymede, and Callisto. To inject some stochastic variation between each moon, yet maintain the 1:2:4 resonance of the inner three, we randomly place each Io analog to have a semimajor axis of  $(a_{SP}/R_P) \sim \mathcal{U}[0.8 \times 6.1, 1.2 \times 6.1]$ , where 6.1 is the actual value for Io around Jupiter and  $\mathcal{U}[a, b]$  is a uniform distribution from  $a \rightarrow b$ . The next moon along is then assumed to lie in a 2:1 resonance, such that  $(a_{SP}/R_P)_{\text{Europa}} = 2^{2/3}(a_{SP}/R_P)_{\text{Io}}$ , and similarly for the Ganymede analog with respect to the Europa analog. The semimajor axis of the Callisto analog, which does not reside in the resonance chain, is then randomly drawn as  $(a_{SP}/R_P)_{\text{Callisto}} \sim \mathcal{U}[3 + a_{SP}/R_P]_{\text{Ganymede}}, 1.2 \times 27.2]$ , where 27.2 is the actual value for Callisto around Jupiter. Any moon systems generated where two moons have semimajor axes within three planetary radii of each other are rejected.

To generate moon radii that are stochastic yet representative, we adopted the radius-separation power-law model of Kane et al. (2013). The authors note that the radii of moons tend to increase with respect to the semimajor axis, following a power-law model. We took the four Galilean moons in isolation and calibrated a least-squares power-law model to it, giving  $\log(R/R_\oplus) \sim \mathcal{N}(6.95 + 0.27 \log(a_{SP}/R_P), 0.17)$ , where the standard deviation quoted is that resulting from the residuals of the best-fitting line. To protect against peculiar draws, we required that the quadrature sum of the radii was within 20% of the actual sum for the Galilean system, the minimum radius moon was at least 80% the radius of Io, and the maximum radius moon was no more than 120% the radius of Ganymede. The resulting covariant distribution is illustrated in Figure 6.

To go from physical radii,  $R_S$ , to  $R_S/R_P$ , needed for the modeling (or equivalently  $R_S/R_\star = (R_S/R_P)(R_P/R_\star)$ ), we

used planetary radii derived in Chen & Kipping (2017b) to make the conversion. We also included the slight TTV and TDV effects induced by the Galilean moons by including  $(M_S/M_P)$ , which was computed by using `forecaster` (Chen & Kipping 2017a) applied to the moon radius to predict a mass, and then using the physical planetary masses predicted in Chen & Kipping (2017b).

The mean longitude of the inner two moons are uniformly, randomly generated, but the third is enforced to satisfy a Laplacian resonance. The inclinations of the moons are randomly drawn from a von Mises distribution with  $\kappa = 42637$ , which we found to maximize the likelihood of a von Mises distribution conditioned on the real Galilean moons. Eccentricities were kept fixed at zero, and the moons all follow perfect Keplerian orbits, i.e., we do not model gravitational interactions between the moons.

After stacking the resulting model light curves with correct cadence and weightings, we tried varying the fraction of systems that harbor moons. Treating each system as a Bernoulli experiment with a probability of having a moon system given by  $\eta$ , we found that varying  $\eta$  was equivalent to simply scaling the  $\eta = 1$  resulting light curve by the same factor. Having demonstrated this, we were able to exploit it to aid in later fits.

In cases where a subset of systems were modeled, the process described above was repeated creating unique model light curves for each specific subset. Generally, the shapes of each resulting light curve were very similar, but ended up with different amplitudes as a result of the differing weights, data gaps, and stellar radii for the host stars. As noted, these factors represent data specific properties for each subset and were saved for later use with the single moon simulations.

#### 6.2.2. Single Moons

While a single moon is four times quicker to generate than four Galilean moons, the Galilean moons follow an expected distribution in terms of their sizes and orbital semimajor axes. For a single hypothetical moon, we have no idea what these properties are, *a priori*, and thus our grid cannot simply span  $\eta$ , as before, but now must also span  $R_S$  and  $a_{SP}$ , leading to a three-dimensional look-up table. Fortunately, the effect of  $\eta$  is a simple scaling, and thus can be applied easily during the fits themselves. However, this still means we need to generate a two-dimensional grid of models, rather than just a single look-up example, in the case of the Galilean analogs.

We set up a logarithmically spaced grid from  $R_S = 0.2 R_\oplus$  to  $R_S = 2.0 R_\oplus$ , with 16 unique grid points. For  $a_{SP}$ , our grid is again logarithmic, defined as  $a_{SP} = 2^x$ , where  $x$  is stepped through from 1 to 7 in 0.1 steps, leading to a total grid size of 976 elements. The moon is treated as being exactly coplanar and circular with random phase. As before, we generate unique light curves for each KOI and then co-add with the appropriate weightings to create our final models. For these simulations, we set  $(M_S/M_P) = 0$  because some simulations permit very massive moons that would cause noticeable TTVs, which would then be subsequently removed anyway by our data-processing pipeline described earlier.

When dealing with subsets, we apply the scaling factors found earlier with the Galilean analog experiments, because the computation time to create the grid required many weeks. During the actual fits, we used a bi-linear interpolation of every unique binned photometric data point, conditioned upon the LUT. We also added an extra grid point of  $R_S = 0.0 R_\oplus$ ,

corresponding to a flat line, to provide numerical stability if fits attempted to compute the likelihood of radii below our  $R_S = 0.2 R_\oplus$  limit.

## 7. Analysis

### 7.1. Galilean Global Fits

We first discuss our results from regressing our photo-dynamical phase-folded planet+moon light curve models (see Section 6) to all 284 KOIs deemed to be of suitable quality for our analysis (see Section 3). As discussed, the fits are conducted for two different light curve models: a Galilean analog and a single moon.

For the Galilean analog, the only parameter directly affecting the light curve model is  $\eta$ , the fraction of KOIs that harbor a Galilean analog. In addition, we added two other free parameters into our fits. The first was to account for excess photometric scatter,  $\sigma$ , and was simply added in quadrature to our derived uncertainties in the planet+stacked light curve. The second was an offset term,  $\gamma$ , to allow for a re-normalization of the data set. While  $\eta$  and  $\gamma$  were assigned uniform priors,  $\sigma$  was assumed to follow a log-uniform prior from 0.1 to 10 ppm. The regression was performed using `MULTINEST` with 1000 live points. The fits were repeated ten times each, from which the posteriors were combined. Because `MULTINEST` estimates the marginal likelihood, we repeated our fits with  $\eta$  fixed to zero and removed as a free parameter, giving us a direct estimate of the Bayes factor,  $B_{SP}$ , for the moon model.

We find that the null model is slightly favored, with  $\log B_{SP} = -0.84$ , or an odds ratio of 2.3:1 in favor of the null model. The resulting light curve and model fitting lines are shown in Figure 7, and the associated posterior distribution is plotted in Figure 8. Our results imply that  $\eta < 0.38$  to 95% confidence for the 284 KOIs considered, with a 68.3% confidence interval of  $\eta = 0.16^{+0.13}_{-0.10}$ .

### 7.2. Single Moon Global Fits

As discussed in Section 6.2.2, the single moon case required on-the-fly interpolation of a look-up table for the likelihood calls. For this reason, we found it more practical to use a Markov Chain Monte Carlo (MCMC) algorithm instead of `MULTINEST`. Our regression was performed using a simple MCMC that we wrote, which used the Metropolis rule for sampling and normal proposal functions tuned by hand to give a  $\sim 50\%$  acceptance rate. Ten independent chains were seeded from random locations within the prior volume, all of which converged within 100 steps and were then allowed to propagate for  $10^5$  accepted steps, giving  $\sim 10^6$  posterior samples in total.

In addition to the three free parameters used in the Galilean fit, we added a parameter controlling the semimajor axis of the moon,  $(a_{SP}/R_P)$ , and the moon size in Earth radii,  $(R_S/R_\oplus)$ . Both were assumed to follow log-uniform priors spanning the limits in our LUT. The  $\eta$  term was allowed to follow a log-uniform prior spanning 0.01 to 100, because it technically represents an effective moon in this case and thus should be interpreted as the average number of moons per system.

The fits converge to a solution of  $R_S = 0.51^{+0.59}_{-0.23} R_\oplus$  and  $(a_{SP}/R_P) = 6.3^{+7.6}_{-3.1}$  for  $\eta = 0.43^{+0.33}_{-0.28}$ . This fit does not directly return a marginal likelihood, because MCMC was used, nor is the Savage-Dickey ratio suitable given that three extra covariant free parameters have been added. However, the

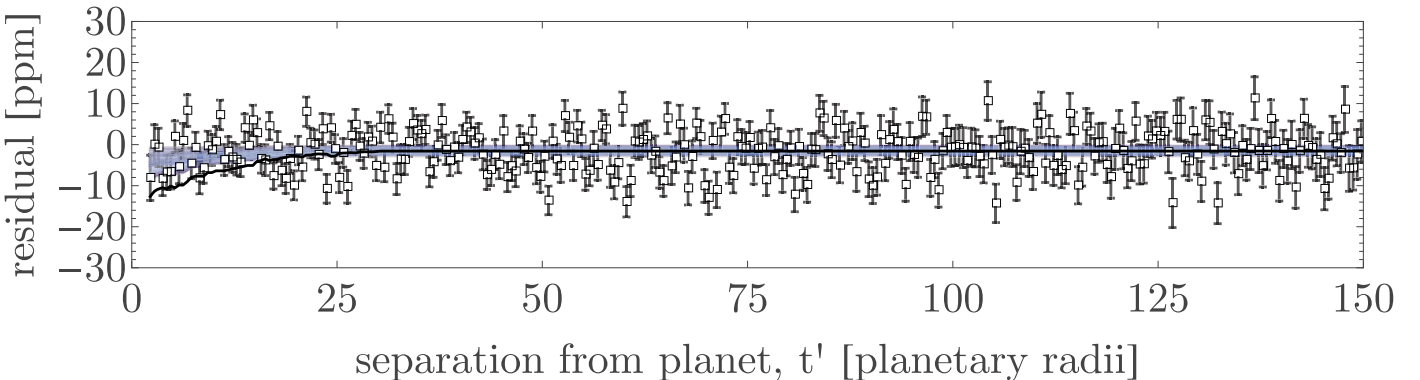


**Figure 7.** Phase-folded planet-stacked light curve of all 284 KOIs deemed to be of acceptable quality. Temporal axis has been re-scaled and binned, with uncertainties shown given by the standard deviations within each bin. Black solid line represents the expected signature if  $\eta = 100\%$  of the KOIs had a Galilean analog moon system. Blue lines show 100 posterior samples from our fits, giving  $\eta = 0.16^{+0.13}_{-0.10}$ .

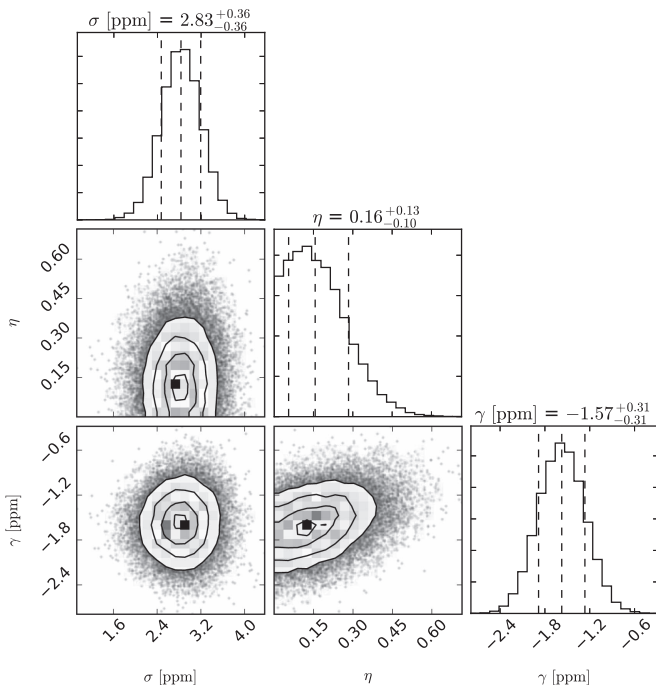


**Figure 8.** Corner plot of the three-parameter joint posterior distribution from our Galilean analog moon fit. This fit was disfavored over a null fit with a Bayes factor of  $B_{SP} = 0.43$ .

kernel-approach shown later reveals that the evidence favoring the single moon fit in this region is modest at  $B_{SP} \simeq 2$ .

### 7.3. Single Moon Kernel

While the single moon fit is useful for identifying the maximum a posteriori region of parameter space, it does not provide a clear view of the overall likelihood trends occurring within the prior volume. To address this, we repeated our fits for a single moon, but fixed  $a_{SP}/R_P$  and  $R_S$  to a specific choice and just regressed  $\eta$ ,  $\sigma$  and  $\gamma$ . Because no interpolation was necessary, it was straightforward to use MULTINEST with  $\eta$ -rescaling on a single interpolated model each time.  $R_S$  was varied across a grid from 0.02 to 2 Earth radii in 100 log-evenly spaced steps. Similarly,  $a_{SP}/R_P$  was varied from 2 to 100, in 100 log-even steps.

At each point, we derive a three-dimensional joint posterior distribution and marginalize over  $\sigma$  and  $\gamma$  to directly measure

the occurrence rate of exomoons at each location. The posterior derived is mathematically equivalent to

$$P(\eta|R_S, a_{SP}/R_P) = \int \int P(\eta, \sigma, \gamma|R_S, a_{SP}/R_P) \times P(\sigma)P(\gamma)d\sigma d\gamma \quad (9)$$

In addition to deriving a posterior at each grid point, we also estimate the evidence against the null model, allowing us to compute the Bayes factor. In Figure 9, we plot the Bayes factor and exomoon frequency for the ensemble as a function of effective moon radius  $R_S$  and semimajor axis  $a_{SP}$ . The Bayes factor (left) indicates whether the moon model is favored over the model without a moon. Red represents regions of parameter space where the moon model is disfavored, while green regions are areas where the moon model is favored, and intensity represents our degree of confidence in that model selection. We emphasize to the reader that paying attention to the contours in this plot is essential for an accurate interpretation; while much of the plot appears green, the moon model is in fact only weakly favored ( $B_{SP} \simeq 2$ ) on a small island in parameter space. By contrast, large values of  $R_S$  and  $a_{SP}$  are strongly ruled out ( $B_{SP}$  around 0.01). A value of 1 in this plot means we can make no statement about one model being a better fit to the data than the other.

The right side of Figure 9 should then be read in the context of the left side. The similarity between the contours on both sides is readily apparent. For large values of  $R_S$  and  $a_{SP}$ , we find an exceptionally low occurrence rate, while the occurrence rate shoots up at the lower end of these variables. It is tempting to read this as a moon signal, but in the context of the Bayes factor on the left, it is clear these occurrence rates are not at all constrained or well-supported by the evidence. Only in regions of high confidence ( $B_{SP}$  much greater or much less than 1) should the exomoon frequency values be given much credence. It is worth pointing out, perhaps, that there is little qualitative difference between a very low exomoon occurrence rate and a very low value for  $B_{SP}$ . Both are consistent with virtually no signal in this region of parameter space.

### 7.4. Evidence for a Population of Super-Ios?

The island on the left side of Figure 9 where  $B_{SP} > 1.50$  is intriguing, if only marginally significant. We hesitate to make any strong statement about this region of parameter space, but it is worth pointing out that theoretical modeling (e.g., Namouni 2010) suggests that, while planets migrating inward

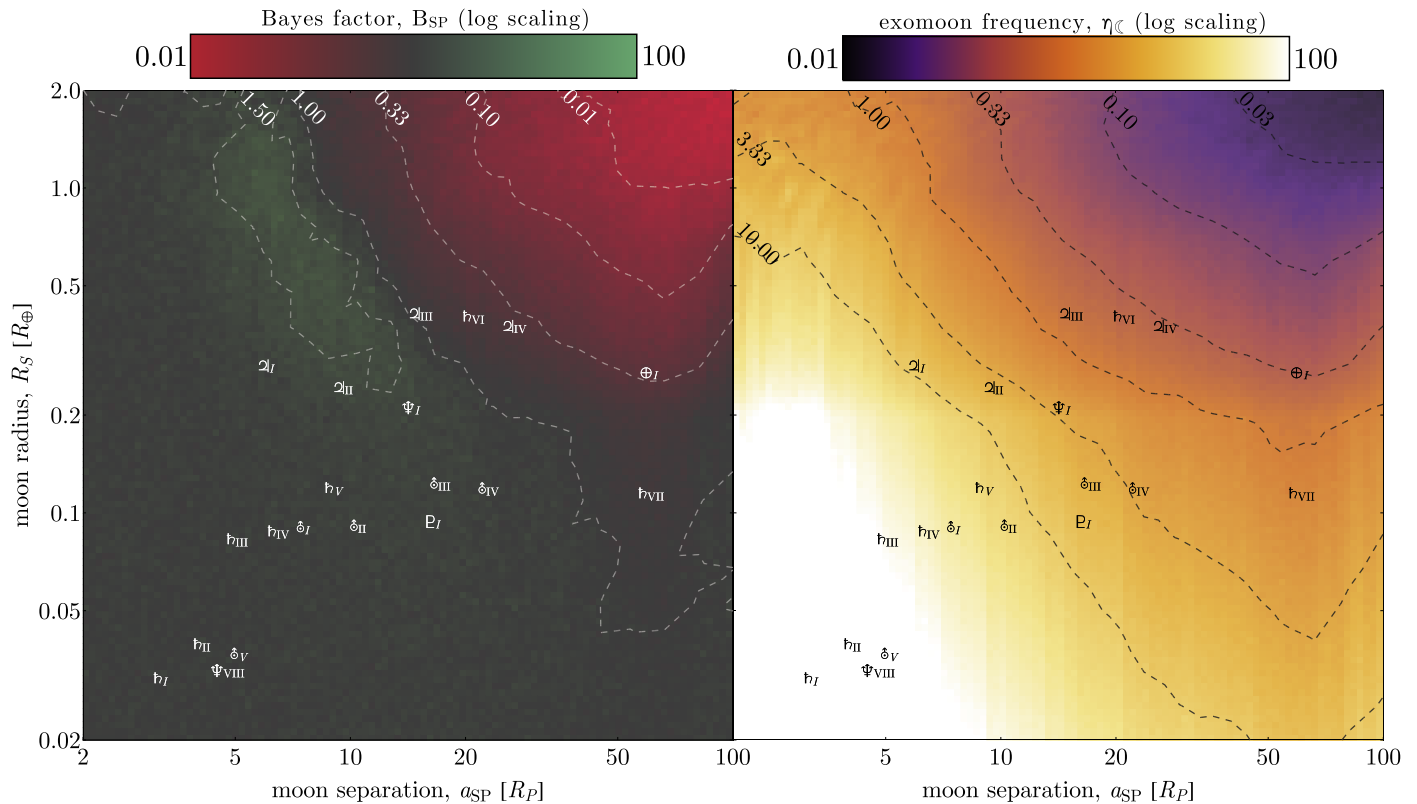


**Figure 9.** Left: heat map of the Bayes factor  $B_{SP}$  as a function of single effective moon radius  $R_S$  and semimajor axis  $a_{SP}$  for the ensemble. Red indicates regions of parameter space where the moon model is disfavored, while green represents regions where the moon model is favored. Greater color intensity corresponds to greater confidence in the selected model. Right: exomoon frequency in the ensemble as a function of  $R_S$  and  $a_{SP}$ . A collection of solar system moons are plotted for context.

will tend to lose their moons in the process due to a shrinking Hill sphere, they are more likely to retain moons orbiting closer to the host planet (that is, close-in moons tend to survive planetary migration to smaller  $a_P$ ). Recall that we are probing planets within roughly 1 au of their host star, suggesting that a large fraction of these planets may have migrated from beyond the snow line. The island of modest moon signal could therefore be evidence (albeit inconclusive) of a population of moons that have survived migration by virtue of their separation from their host planet. Note, however, that more recent theoretical work (Spalding et al. 2016) suggests, by contrast, that satellites closer in to their planet ( $a_{SP} \lesssim 10 R_P$ ) are also vulnerable to dynamical moon-loss during migration. It is unclear, then, whether one or both of these mechanisms could be at play here, and indeed, the strength of these mechanisms relies in part of the evolutionary history of each system—which will, of course, be unique. In any case, our results suggesting a dearth of exomoons at small  $a_P$  appear to provide observational support for the findings of both Namouni (2010) and Spalding et al. (2016), and more broadly, could be evidence of giant planet migration.

### 7.5. Subset Fits

In addition to fitting the entire sample with effective moon and Galilean analog GLC models, we also performed GLC fits on a number of physically motivated subsets. The aim here was to identify whether a certain class of planets in the sample preferentially hosts moons over another. As such, we divided the sample into several equally populated pairs and fit the GLC model to these subsets. These pairs were small/large planets, cold/hot planets, cold/hot stars, and inner/outer planets. We

also split the sample into single/multi-planet systems, and habitable zone/non-habitable zone planets (most of the latter residing inside the innermost edge of the habitable zone). These last two categories, of course, are not equally populated. Insolations were taken from [the NASA Exoplanet Archive](#), and anything less than the maximum (inner-edge) insolation given in Yang et al. (2014) Equation (2) was considered to be in the habitable zone.

The results for Galilean moon fits can be seen in Figure 10 and Table 1. The thick black line in the figure represents the peak posterior value, while the light red lines represent 50 fair draws from the posterior. From these plots, we can make a number of comparisons. Dividing the sample in two by size, we see a marginally higher occurrence rate for the larger planets. For planet temperature, we see a higher occurrence rate on the colder end. We also see a higher exomoons occurrence rate for colder stars, which we can take to mean later-type or evolved stars. All of these observations are in line with what we might expect a priori.

We see very little difference in the occurrence rate for single- and multi-planet systems. Interestingly, though, the inner 50% of planets (those closest to their star) show a significantly higher exomoon occurrence rate than those farther away, where the maximum a posteriori value indicates a total non-detection. This is unexpected because the Hill sphere shrinks with smaller semimajor axis. Finally, and perhaps most intriguingly, the maximum a posteriori values for habitable zone planets ran away to the maximum, while non-habitable zone planets have a much lower occurrence rate. This should be read with caution, however, considering the size of the error bars in the habitable zone planet case. While the comparisons above are made

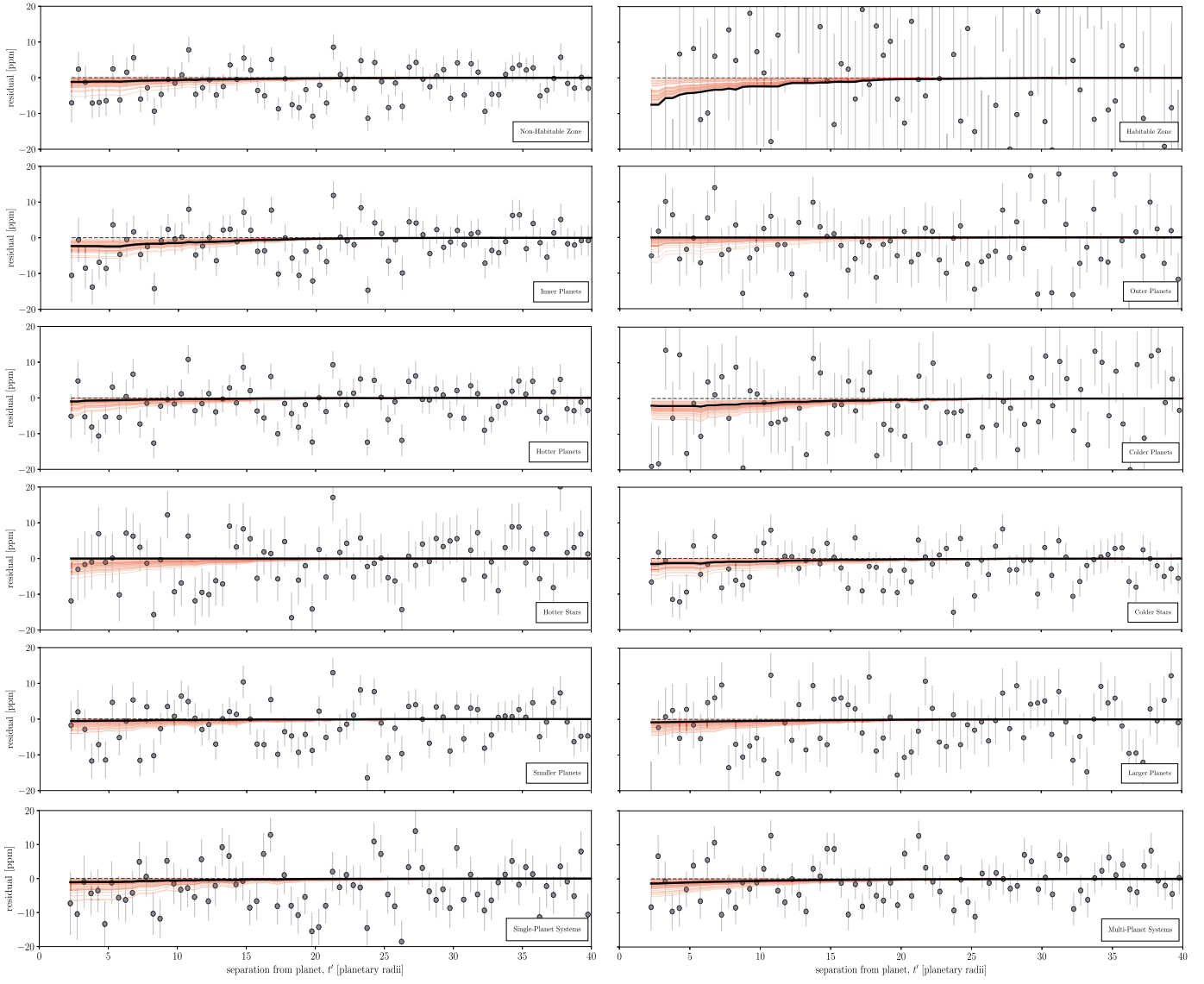


**Figure 10.** Galilean analog GLC plots for a variety of sample subsets.

between equally populated subsets, there are far more non-habitable zone planets than there are planets in the habitable zone, making the results in the latter case far more uncertain.

Single, effective moon fits were also performed for these same OSE subsets. Results can be found in Table 2. Unlike the case for Galilean analog fits, we cannot meaningfully quote an occurrence rate in this case because the depth of the moon signal is controlled by the size of the effective moon. There is a degeneracy between moon size and occurrence rate, so we model the size of the moon as a proxy for occurrence rate. In essence, a smaller effective moon can mean either (a) we have a high occurrence rate of small moons, or (b) we have a low occurrence rate of larger moons. The truth, of course, is probably somewhere in the middle.

To characterize whether our fits exclude a null detection to high confidence we compute the Savage-Dickey ratio between a uniform prior and the posterior distribution for  $R_S^2 = 0$ . We treat this number as our Bayes factor. For the colder stars, we find  $B_{SP} = 1.53$ , for outer planets  $B_{SP} = 0.7$ , large planets  $B_{SP} = 1.29$ , multi-planet systems  $B_{SP} = 0.77$ , and habitable zone planets  $B_{SP} = 3.11$ . These values suggest that there is

only marginal evidence in support of an effective moon signal in the cold star, large planet, and habitable zone planet subsets, while the null hypothesis is favored for the outer planet and multi-planet subsets.

## 8. Exomoon Candidate Kepler-1625b I

### 8.1. Individual Fits

Thus far, our analysis has taken a population-based approach to seeking exomoons, in contrast to the conventional method adopted in previous HEK papers where candidates were interrogated individually. Although a full suite of photodynamical Bayesian fits to each planetary candidate is beyond the scope of this work, representing a formidable computational challenge, we do here investigate systems individually with a simpler model.

For each KOI, we took the final phase-folded light curve and used MULTINEST to fit the Heller (2014) OSE model through the data. As discussed earlier, OSE does have drawbacks, yet it remains a useful and quick tool for checking for any significant flux decreases surrounding the phase-folded transits. For each

**Table 1**  
Table of Occurrence Rates  $\eta$  for Various Subsets of the 284 Planets Examined in This Work

Galilean Analog Subset Fits							
Group	$\eta_{\mathbb{C}} [1\sigma]$	$\eta_{\mathbb{C}}^{\max} [2\sigma]$	$B_{SP}$	Group	$\eta_{\mathbb{C}} [1\sigma]$	$\eta_{\mathbb{C}}^{\max} [2\sigma]$	$B_{SP}$
Smaller Planets	[0.06, 0.35]	0.48	$0.353 \pm 0.035$	Larger Planets	[0.07, 0.44]	0.61	$0.448 \pm 0.035$
Colder Planets	[0.15, 0.68]	0.86	$1.003 \pm 0.070$	Hotter Planets	[0.07, 0.39]	0.53	$0.426 \pm 0.043$
Colder Stars	[0.07, 0.33]	0.44	$0.639 \pm 0.063$	Hotter Stars	[0.06, 0.47]	0.66	$0.411 \pm 0.034$
Inner Planets	[0.21, 0.64]	0.80	$2.564 \pm 0.250$	Outer Planets	[0.03, 0.28]	0.42	$0.224 \pm 0.018$
Single-Planet Systems	[0.08, 0.50]	0.68	$0.689 \pm 0.066$	Multi-Planet Systems	[0.07, 0.33]	0.44	$0.420 \pm 0.038$
Habitable Zone	[0.23, 0.88]	0.97	$1.679 \pm 0.083$	Non-habitable Zone	[0.08, 0.37]	0.50	$0.653 \pm 0.066$

**Note.** Here,  $\eta$  represents  $1\sigma$  credible interval values from the posterior distributions, 95 pct is the 95th percentile upper limit, and  $B_{SP}$  is the Bayesian evidence computed by MULTINEST.

KOI, we fit for an offset term, a photometric jitter, the moon size, and a semimajor axis, ( $a_{SP}/R_P$ ) with MULTINEST using 1000 live points. In the earlier ensemble fits, we used a log-uniform prior on the moon-size (see Section 7.1), which means negative moon radii cannot be sampled. In these fits, we wished to allow for negative radius moons, which correspond to inverted transit signals, to provide insights into possible biases affecting the results. Accordingly, we modified our moon parameter to be the satellite-to-star ratio-of-radii,  $s$ , squared, to account for the fact that transit detection bias is approximately proportional to  $s^2$ .

We evaluated the median  $s^2$  value for each KOI from the posterior chain and divided by the lower quantile, bounding a 68.3% confidence interval, a metric we loosely refer to as “significance” in what follows (although it is best interpreted as a power). In Figure 11, we show a histogram of the resulting significances for 353 KOIs, where we have also included the likely eccentric KOIs to provide a wider sample to assess distribution properties. Inspection of the results reveals a sizable spread centered around zero, as might be expected. However, we note that KOI-5084.01 (Kepler-1625b) appears quite deviant from the bulk population, with a  $+4.4\sigma$  significance. Similarly, KOI-4202.01 (Kepler-1567b) is an outlier on the negative scale with a  $-4.4\sigma$  significance.

The negative outlier clearly cannot be a genuine exomoon, and thus we do not consider it further in what follows. The positive outlier, though, could be an isolated candidate missed by the ensemble analyses. Excluding the two outliers, the histogram shown in Figure 11 is well-described by a normal distribution centered on zero with a standard deviation of 0.8. If we generate a list of 353 random variates from that distribution and take the maximum value,  $+4.4$  is highly improbable; we used Monte Carlo simulations to estimate the probability, which was found to be  $4 \times 10^{-6}$ . On this basis, Kepler-1625b appears quite unexpected and thus worthy of more detailed investigation.

### 8.2. Detailed Investigation of Kepler-1625b

To investigate further, we performed detailed photodynamical fits of Kepler-1625b using the LUNA model and MULTINEST, in the same manner as that conducted in our previous series of HEK papers (e.g., see Kipping et al. 2013b). This enables a rigorous Bayesian model selection to ensure not only a physically plausible model that can explain the photometry, but also that the moon parameters are justified given the extra complexity they introduce.

Comparing the evidences between a planet-only and planet+moon model revealed that the moon model was favored with  $\log B_{SP} = 10.2$ , or a  $4.1\sigma$  preference, consistent with the level found previously. The light curve fits are illustrated in Figure 12.

Given the limited number of transits available (only three), the conventional HEK approach of cross-validating by removing a transit was not tenable, and thus we adapted this strategy somewhat in what follows. Instead, we performed  $k$ -fold cross-validations, where we omit one half of a transit (centered about the time of inferior conjunction) and re-fit the remaining data blindly each time. Because there are three transits in the *Kepler* data, this yields six unique ways of conducting the cross-validation. In each case, we performed a new blind fit and found a positive detection consistent with the original signal in all cases, with Bayes factors indicating 3.9, 2.4, 4.6, 4.0, 3.1, and  $2.7\sigma$  preference for the moon model (comparable to the original  $4.1\sigma$  detection when using all of the data).

As with all previous moon candidates, we attempted to rule out all other possible explanations for the signal. For any candidate moon signal, there will be one of two possible explanations: the signal is either an instrumental artifact or it has a true astrophysical origin (be it an exomoon or something else). To test the possibility of an instrumental aberration, we performed an independent and manual detrending on the *Kepler* DR25 data (our OSE survey used DR24) using CoFiAM on the PA and PDC data. In both cases, the planet-moon model remained the favored hypothesis over the planet-only model. In contrast, polynomial-based detrending was found to remove the signal, likely due to the very long timescale of the driving event occurring in epoch three.

We also examined data from individual *Kepler* pixels to determine whether there might have been anomalous behavior in the vicinity of the transit events (as occurred for false positive Kepler-90g.01; Kipping et al. 2015b), but no unusual spikes or drop-outs were detected in any relevant pixel. We also verified that there were no bad data flags at the time of the transits, which was a source of the false positive result for the moon candidate around PH2-b (Kipping et al. 2015a).

If the signal were astrophysical in origin, then there are several possible hypotheses, including a moon. A ring is not likely because it should produce a coherent signal in all events, which is not seen, unless the ring precession rate is very fast. Rotating spots on the surface of the star also affect the light curve, primarily producing a long-term undulation in the data. This long-term trend is removed via our detrending (repeated several times independently) and thus the only remaining

**Table 2**  
Table of Effective Moon Sizes  $R_S$  for Various Subsets of the 284 Planets Examined in this Work, in Units of Earth Radii

Single Effective Moon Subset Fits							
Group	$R_S [1\sigma]$	$R_S^{\max} [2\sigma]$	$B_{SP}$	Group	$R_S [1\sigma]$	$R_S^{\max} [2\sigma]$	$B_{SP}$
Smaller Planets	[0.02, 0.36]	0.90	0.75	Larger Planets	[0.02, 0.41]	1.18	0.76
Colder Planets	[0.02, 0.41]	1.12	0.81	Hotter Planets	[0.02, 0.42]	1.03	0.79
Colder Stars	[0.02, 0.35]	0.83	0.79	Hotter Stars	[0.02, 0.36]	1.07	0.74
Inner Planets	[0.03, 0.81]	1.40	1.04	Outer Planets	[0.02, 0.29]	0.83	0.69
Single-Planet Systems	[0.02, 0.42]	1.05	0.79	Multi-Planet Systems	[0.02, 0.34]	0.96	0.72
Habitable Zone	[0.03, 1.10]	1.66	1.12	Non-habitable Zone	[0.02, 0.33]	0.92	0.74

**Note.** We present  $1\sigma$  credible interval values from the posterior distributions, while 95 pct is the 95th percentile upper limit. Here,  $B_{SP}$  is the Savage-Dickey ratio computed from the  $\log(R_S)$  posteriors.

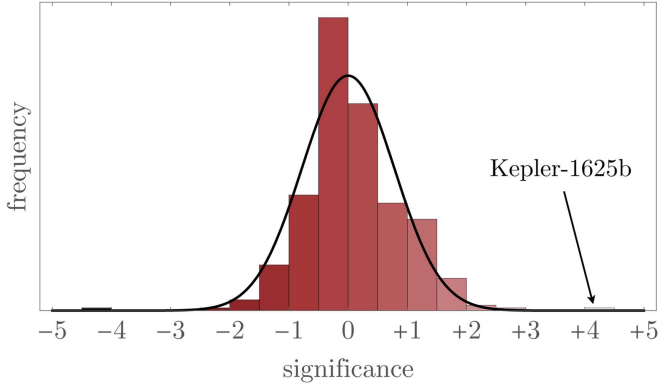


**Figure 11.** Histogram of the “significance” of an OSE detection for several hundred KOIs, the test that revealed the presence of a possible candidate around Kepler-1625b. The vertical axis scale is linear.

possible starspot-induced signal would be crossing events. However, starspot crossings (when a transiting planet occults a dark spot; e.g., see Rabus et al. 2009) cannot be responsible for the observed moon-like dips. This is because spot crossings can only occur inside the main planetary transit and can never produce out-of-transit flux decreases, as seen for Kepler-1625b, purely from a geometrical argument. If the signal were confirmed then, this would leave the exomoon hypothesis as the leading explanation based on current information.

The quoted stellar properties of Kepler-1625 in the [NASA Exoplanet Archive](#) changed significantly from DR24 to DR25, owing to the addition of updated information in the latter data release (Mathur et al. 2017). This update pushed the star from a sub-solar to a super-solar radius ( $R_* = 0.838^{+0.366}_{-0.079} \rightarrow 1.793^{+0.263}_{-0.488} R_\odot$ ), enhanced the metallicity from sub- to super-solar abundances, and lowered the density substantially ( $\rho_* = 2.059^{+0.4626}_{-1.306} \rightarrow 0.2636^{+0.3257}_{-0.0768} \text{ g cm}^{-3}$ ), indicating that this star is likely climbing the giant branch. Critically, our planet-only and planet+moon fits favor a low stellar density of  $\rho_* = 0.387^{+0.034}_{-0.083} \text{ g cm}^{-3}$  and  $\rho_* = 0.405^{+0.028}_{-0.054} \text{ g cm}^{-3}$ . If the true density were much higher, then Kepler-1625b would need to be either highly eccentric or blended (Kipping 2014), both of which would be severely detrimental to the exomoon hypothesis. Determining the true nature of this star is critical as it will also dictate the sizes of the planet and moon derived from the transit depth (which we describe shortly).

We also attempted to recover a rotation period for the star (following the methodology described in Torres et al. 2015) but the amplitude of variability appears too small to recover a consistent period across each quarter, with best-fitting periods

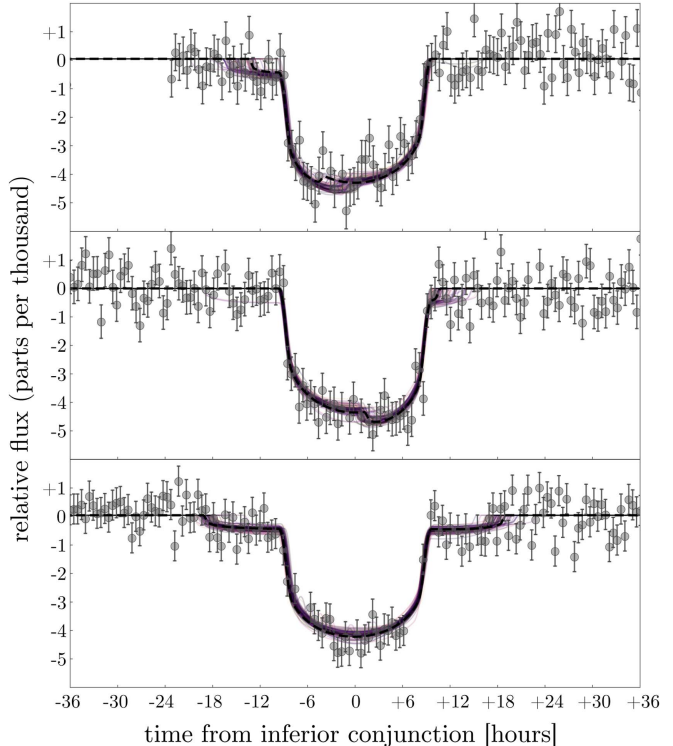


**Figure 12.** The three transits of Kepler-1625b observed with *Kepler*, overlaid with 100 draws from the model posteriors. The black line is the maximum a posteriori model.

ranging from 4.5 days to 21 days. Attempting to regress a coherent signal across all quarters gives an amplitude of 66 ppm; when performed on each quarter independently, the median amplitude was 136 ppm. Given the lack of strong evidence for rotation, the weak amplitudes in comparison to the candidate moon transit depth (570 ppm), and the arguments made earlier as to why rotational modulations are unlikely to be a source of false-positive, we deem it unlikely that activity is responsible for the signal observed.

Our photodynamical fits, combined with the DR25 stellar properties indicate that Kepler-1625b is likely a Jupiter-sized planet with approximately ten times Jupiter’s mass, orbited by a moon roughly the size of Neptune. We calculate the radii of the planet and moon by measuring the depth of the flux dip ( $\Delta F/F = (R_o/R_*)^2$ , where  $R_o$  is the radius of the object in question) and we are able to derive a mass based on the photodynamical model fit. We note that both the planet and the moon show good agreement between mass and radius estimates

and lie in physically reasonable parameter space based on the mass–radius forecaster model of Chen & Kipping (2017a). We find the semimajor axis of the moon  $a_S = 19.1^{+2.1}_{-1.9} R_P$ , which is well outside the Roche limit and comfortably within the Hill sphere for this planet. It is dynamically stable and should not have spun out/escaped over 5 Gyr (Barnes & O’Brien 2002).

While the existence of a Neptune-sized moon has largely not been anticipated in the literature (however, see Cabrera & Schneider 2007), we cannot readily rule out its existence on these grounds. Indeed, the existence of Hot Jupiters was also wholly unexpected prior to their discovery in the mid-1990s. It seems clear that a moon of this type could not have formed in a circumplanetary accretion disk akin to that which is thought to have formed the regular moons of Jupiter and Saturn. It is conceivable, however, that the moon could have been captured by the planet, a kind of intermediate process between typical capture scenarios (e.g., Neptune and Triton; see Agnor & Hamilton 2006) and the cataclysmic impact event that is believed to have formed Earth’s Moon (Ćuk & Stewart 2012). In this scenario, a grazing impact might be experienced as a kind of extreme atmospheric drag sufficient to capture the passing body. Observation of this system might therefore not only produce the first unambiguous detection of an exomoon, but could also go a long way in demonstrating once again that what we observe in our solar system is not all that is possible.

### 8.3. Validating the Exomoon Candidate Kepler-1625b I

At this time, we remain cautious about the reality of this signal, given the relatively small number of transits available. This is particularly true because the third transit appears to be crucial to the exomoon interpretation and can be removed using polynomial-based detrending approaches. Detrending the photometric time series of long-period transits is more challenging than for their shorter-period counterparts, and it remains wholly plausible that the signal observed is nothing more than an artifact of our detrending process. We strongly emphasize these points and encourage the community not to treat this signal as genuine until it can be confirmed.

Fortunately, our photodynamic moon fit yields a testable prediction for the morphology of the next transit event occurring 2017 October. With such a long event duration from anticipated exomoon ingress to egress, the event cannot be observed in its entirety by any single optical/NIR instrument on the ground south of latitude  $\sim 78^\circ$  N (north of which the long Arctic night has already begun on the date of observation). A space-based observation is clearly essential to characterize the system. We have therefore secured *HST* observations to validate the signal during the next transit of the planet, and we strongly advocate treating this object as no more than a candidate at this time, similar to previous moon candidates discussed in earlier HEK papers.

## 9. Conclusion

In this work, we have examined 284 *Kepler* exoplanets (from an original sample of 4098 KOIs) in search of an exomoon signal in the ensemble. We performed a rigorous multi-stage analysis to select only the highest quality data, measure and correct for TTVs, and stack a total of 6096 transit events to characterize the exomoon population. As a byproduct of our work, we present new TTV posterior distributions, along with a handful of stellar properties, and make them available online to the community.

Our results place new upper limits on the exomoon population for planets orbiting within about 1 au of their host star—upper limits that are remarkably low. We have also analyzed subsets of the ensemble to test the effect of various data cuts. Our analysis suggests that exomoons may be quite rare around planets at small semimajor axes, a finding that supports theoretical work suggesting moons may be lost as planets migrate inward. On the other hand, if the dearth of exomoons can be read as a reliable indicator of migration, our results suggest a large fraction of the planets in the ensemble have migrated to their present location.

Finally, we have briefly highlighted our identification of an exomoon candidate in the Kepler-1625 system, for which we have secured a follow-up observation with *HST*. This candidate has passed a thorough preliminary inspection, but we emphasize again our position that the *Kepler* data are insufficient to make a conclusive statement about the existence of this moon. Only after the *HST* observation is made should any claim about this moon’s existence be given much credence.

This paper includes data collected by the *Kepler* mission. Funding for the *Kepler* mission is provided by the NASA Science Mission directorate.

Resources supporting this work were provided by the NASA High-End Computing (HEC) Program through the NASA Advanced Supercomputing (NAS) Division at Ames Research Center.

This research has made use of the NASA Exoplanet Archive, which is operated by the California Institute of Technology, under contract with the National Aeronautics and Space Administration under the Exoplanet Exploration Program.

This research has made use of the `corner.py` code by Dan Foreman-Mackey at <http://github.com/dfm/corner.py>.

This work made use of the Michael Dodds Computing Facility, for which we are grateful to Michael Dodds, Carl Allegretti, David Van Buren, Anthony Grange, Cameron Lehman, Ivan Longland, Dell Lunceford, Gregor Rothfuss, Matt Salzberg, Richard Sundvall, Graham Symmonds, Kenneth Takigawa, Marion Adam, Dour High Arch, Mike Barrett, Greg Cole, Sheena Dean, Steven Delong, Robert Goodman, Mark Greene, Stephen Kitt, Robert Leyland, Matthias Meier, Roy Mitsuoka, David Nicholson, Nicole Papas, Steven Purcell, Austen Redman, Michael Sheldon, Ronald Sonenthal, Nicholas Steinbrecher, Corbin Sydney, John Vajgrt, Louise Valmoria, Hunter Williams, Troy Winarski, and Nigel Wright.

We thank members of the Cool Worlds Lab for helpful conversations in preparing this manuscript. Finally, we thank the anonymous referees for their constructive comments. D.M.K. acknowledges support from NASA grant NNX15AF09G (NASA ADAP Program). A.T. acknowledges support from the NSF GRFP grant DGE 16-44869.

## ORCID iDs

- A. Teachey  <https://orcid.org/0000-0003-2331-5606>
- D. M. Kipping  <https://orcid.org/0000-0002-4365-7366>
- A. R. Schmitt  <https://orcid.org/0000-0002-5034-0949>

## References

- Adams, E. R., Ciardi, D. R., Dupree, A. K., et al. 2012, *AJ*, 144, 42
- Adams, E. R., Dupree, A. K., Kulesa, C., & McCarthy, D. 2013, *AJ*, 146, 9
- Agnor, C., & Hamilton, D. P. 2006, *Natur*, 441, 192
- Agol, E., Steffen, J., Sari, R., & Clarkson, W. 2005, *MNRAS*, 359, 567

- Akeson, R. L., Chen, X., Ciardi, D., et al. 2013, *PASP*, **125**, 989  
 Barnes, J. W., & O'Brien, D. P. 2002, *ApJ*, **575**, 1087  
 Bennett, D. P., Batista, V., Bond, I. A., et al. 2014, *ApJ*, **785**, 155  
 Cabrera, J., & Schneider, J. 2007, *A&A*, **464**, 1133  
 Canup, R. M., & Ward, W. R. 2002, *ApJ*, **124**, 3404  
 Canup, R. M., & Ward, W. R. 2006, *Natur*, **441**, 834  
 Carter, J. A., Fabrycky, D. C., Ragozzine, D., et al. 2011, *Sci*, **331**, 562  
 Chen, J., & Kipping, D. M. 2017a, *ApJ*, **834**, 17  
 Chen, J., & Kipping, D. M. 2017b, *MNRAS*, in press (arXiv:1706.01522)  
 Christiansen, J. L., Jenkins, J. M., Caldwell, D. A., et al. 2012, *PASP*, **124**, 1279  
 Ćuk, M., & Stewart, S. T. 2012, *Sci*, **338**, 1047  
 Dawson, R. I., & Johnson, J. A. 2012, *ApJ*, **756**, 122  
 Dickey, J. O., Bender, P. L., Faller, J. E., et al. 1994, *Sci*, **265**, 482  
 Domingos, R. C., Winter, O. C., & Yokoyama, T. 2006, *MNRAS*, **373**, 1227  
 Dressing, C. D., Adams, E. R., Dupree, A. K., Kulesa, C., & McCarthy, D. 2014, *AJ*, **148**, 78  
 Durbin, J., & Watson, G. S. 1950, *Biometrika*, **37**, 409  
 Everett, M. E., Barclay, T., Ciardi, D. R., et al. 2015, *AJ*, **149**, 55  
 Feroz, F., & Hobson, M. P. 2008, *MNRAS*, **384**, 449  
 Feroz, F., Hobson, M. P., & Bridges, M. 2009, *MNRAS*, **398**, 1601  
 Gong, Y.-X., Zhou, J.-L., Wie, J.-W., & Wu, X.-M. 2013, *ApJL*, **769**, L14  
 Gould, A., Gaudi, S. B., & Han, C. 2004, arXiv:astro-ph/0405217  
 Hansen, C. J., Esposito, L., Stewart, A. I. F., et al. 2006, *Sci*, **311**, 1422  
 Hansen, C. J., Hendrix, A., Esposito, L., et al. 2005, AGU FM, #P21F-04  
 Heller, R. 2014, *ApJ*, **787**, 14  
 Heller, R., Hippke, M., & Jackson, B. 2016, *ApJ*, **820**, 88  
 Hippke, M. 2015, *ApJ*, **806**, 51  
 Hogg, D. W., Myers, A. D., & Bovy, J. 2010, *ApJ*, **725**, 2166  
 Holezer, T., Mazeh, T., Nachmani, G., et al. 2016, *ApJS*, **225**, 9  
 Holman, M. J., & Murray, N. W. 2005, *Sci*, **307**, 1288  
 Huber, D., Silva, A. V., Matthews, J. M., et al. 2014, *ApJS*, **211**, 2  
 Ida, S., Canup, R. M., & Stewart, G. R. 1997, *Natur*, **389**, 353  
 Kane, S. R., Hinkel, N. R., & Raymond, S. N. 2013, *AJ*, **146**, 122  
 Kipping, D. M. 2009a, *MNRAS*, **392**, 181  
 Kipping, D. M. 2009b, *MNRAS*, **396**, 1797  
 Kipping, D. M. 2010a, *MNRAS*, **407**, 301  
 Kipping, D. M. 2010b, *MNRAS*, **408**, 1758  
 Kipping, D. M. 2011, *MNRAS*, **416**, 689  
 Kipping, D. M. 2013, in Proc. Frank N. Bash Symp 2013: New Horizons in Astronomy (Trieste: Proceedings of Science), **12**  
 Kipping, D. M. 2013, *MNRAS*, **435**, 2152  
 Kipping, D. M. 2014, *MNRAS*, **440**, 2164  
 Kipping, D. M., Bakos, G. Á., Buchhave, L. A., Nesvorný, D., & Schmitt, A. R. 2012, *ApJ*, **750**, 115  
 Kipping, D. M., Dunn, W. R., Jasinski, J. M., & Manthri, V. P. 2012, *MNRAS*, **421**, 1166  
 Kipping, D. M., Forgan, D., Hartman, J., et al. 2013b, *ApJ*, **777**, 134  
 Kipping, D. M., Hartman, J., Buchhave, L. A., et al. 2013a, *ApJ*, **770**, 101  
 Kipping, D. M., Huang, X., Nesvorný, D., et al. 2015b, *ApJL*, **799**, L14  
 Kipping, D. M., Nesvorný, D., Buchhave, L. A., et al. 2014, *ApJ*, **784**, 28  
 Kipping, D. M., Schmitt, A. R., Huang, X., et al. 2015a, *ApJ*, **813**, 14  
 Kipping, D. M., & Tinetti, G. 2010, *MNRAS*, **407**, 2589  
 Kolbl, R., Marcy, G. W., Isaacson, H., & Howard, A. W. 2015, *AJ*, **149**, 18  
 Kovács, G., Zucker, S., & Mazeh, T. 2002, *A&A*, **391**, 369  
 Kozai, Y. 1968, *PASJ*, **20**, 24  
 Kundurthy, P., Agol, E., Becker, A. C., et al. 2011, *ApJ*, **731**, 123  
 Lainey, V., Arlot, J.-E., Karatekin, Ö., et al. 2009, *Natur*, **459**, 957  
 Lainey, V., Karatekin, Ö., Desmars, J., et al. 2012, *ApJ*, **752**, 14  
 Law, N. M., Morton, T., Baranec, C., et al. 2014, *ApJ*, **791**, 35  
 Mathur, S., Huber, D., Batalha, N. M., et al. 2017, *ApJS*, **229**, 30  
 Mayor, M., & Queloz, D. 1995, *Natur*, **378**, 355  
 Morabito, L. A., Synnott, S. P., Kupferman, P. N., & Collins, S. A. 1979, *Sci*, **204**, 972  
 Namouni, F. 2010, *ApJL*, **719**, L145  
 Rabus, M., Alonso, R., Belmonte, J. A., et al. 2009, *A&A*, **494**, 391  
 Sartoretti, P., & Schneider, J. 1999, *A&AS*, **134**, 553  
 Seager, S., & Mallén-Ornelas, G. 2003, *ApJ*, **585**, 1038  
 Sheets, H. A., & Deming, D. 2014, *ApJ*, **794**, 133  
 Simon, A. E., Szabó, Gy. M., Kiss, L. L., & Szatmáry, K. 2012, *MNRAS*, **419**, 164  
 Smith, J. C., Stumpe, M. C., Van Cleve, J. E., et al. 2012, *PASP*, **124**, 1000  
 Spalding, C., Batygin, K., & Adams, F. C. 2016, *ApJ*, **817**, 18  
 Sparks, W. B., Hand, K. P., McGrath, M. A., et al. 2016, *ApJ*, **829**, 121  
 Squyres, S. W., Reynolds, R. T., & Cassen, P. M. 1983, *Natur*, **301**, 225  
 Stumpe, M. C., Smith, J. C., Van Cleve, J. E., et al. 2012, *PASP*, **124**, 985  
 Torres, G., Kipping, D. M., Fressin, F., et al. 2015, *ApJ*, **800**, 99  
 Trafton, L. 1974, *ApJ*, **193**, 477  
 Waldmann, I. P., Tinetti, G., Drossart, P., et al. 2012, *ApJ*, **744**, 35  
 Yang, J., Boué, G., Fabrycky, D. C., & Abbot, D. S. 2014, *ApJL*, **787**, L2